Study for the feasibility of fluidized bed membrane reactors: membrane supports reutilization and hydrodynamics at high temperature

Research project

Presented to the Multiphase Reactors Group

and the Faculty of Chemical Engineering and Chemistry

Eindhoven University of Technology

by Cristina Herrero

February 13, 2017

Graduation Committee

Prof. dr. ir. M. van Sint Annaland

Dr. F. Gallucci

Ir. J. A. Medrano Jimenez

Abstract

Membrane reactors can bring various potential advantages in terms of efficiency and economics for H_2 production compared to the benchmark technology based on the Fired Tubular Reforming plant. However, for further implementation at industrial scale still some different aspects should be studied and investigated more in depth, especially those with an important impact on the economics of the process.

Membrane costs are still high and can represent up to 15% of the total capital costs in a large scale production plant. A main responsible of these high costs is the high price of the support material (Hastelloy-X). To enhance the success of membrane reactors for hydrogen production, the present work focuses on the study of the reutilization of metallic supported Pd-Ag membrane for high temperature applications, especially by focusing on the reutilization of the support material. In this work, a metallic supported Pd-Ag membrane has been reutilized and tested after continuous operation under high temperatures for more than 1200 h. According to N_2 permeance tests done during the characterization of the support for the original membrane and the repaired one, the metallic support might have suffered some sintering during long-term test. Furthermore, part of the ceramic layer of the fresh support membrane remained after the embrittlement, and thus this layer might have become thicker. The repaired membrane has been tested for more than 700 h and lower hydrogen perm-selectivities than in the original membrane are obtained, as well as an expected decrease in permeance. The membrane has also been tested under the influence of different parameters for water gas shift reaction conditions. It has been demonstrated that there is no interaction of the Pd-Ag layer with the $Ni/CaAl_2O_4$, thus resulting in a constant permeance in the fluidized bed membrane reactor. However, a catalytic effect of the support material (Inconel) has been observed due to the high CO conversions, besides the effect of the catalyst used.

Furthermore, to better understand the behaviour of membrane reactors, especially the fluidized bed membrane reactor concept, better closure equations are needed to describe the fluid-dynamic behaviour of this concept at reacting conditions. In this work, it is aimed to extend a recently fundamental research carried out by Mustafa Taşdemir [1] for fluidized beds at room temperature, who developed a correlation to predict solids movement inside fluidized beds as function of bubble properties using novel optical LED-PIV/DIA techniques. This implies to apply this findings to the recently developed technique to study the hydrodynamic characteristics of fluidized beds at high temperatures, ePIV/DIA. To do so, LED-PIV/DIA and ePIV/DIA techniques are compared at room temperature, resulting in an overestimation of the bubble diameter and an underestimation of the solids hold-up when using the endoscopic technique. It might be related to the larger interrogation area used to treat ePIV/DIA recordings, besides the fact that the endoscope reduces the intensity of the laser hampering the detection of the smallest bubbles and averaging the larger ones. Furthermore, it is located in a corner resulting in a weak illumination at the top and bottom right corners and thus, an underestimation of the solids hold-up is found. The deviations observed between both techniques result in a difficult fitting of theoretical and experimental results at high temperature, hindering the extension of the novel correlation.

Contents

Nomenclature

Symbol	**Definition**	**Unit**
A	Area	m^2
Ar	Archimedes number	-
C	Concentration	mol/m^3
D	Diffusion coefficient	m^2/s
d	Diameter	m
E_a	Activation energy	J/mol
e	Endoscope	
FBR	Fluidized bed reactor	
FBMR	Fluidized membrane reactor	
f	Fraction	-
g	Gravitational constant	m/s^2
h	Height above distributor plate	m
J	Permeation	$\frac{mol}{m^2 * s}$
K	Mass transfer coefficient	s^{-1}
L	Permeability	$\frac{mol * m}{m^2 * s * Pa^n}$
L_0	Pre-exponential factor	$\frac{mol * m}{m^2 * s * Pa^n}$
M	Molar mass	g/mol
n	Pressure exponent	-
p	Pressure	Pa
px	Pixel	
R	Ideal gas constant	
r	Reaction rate	$\frac{mol}{kg_{cat} * s}$
Rt	Peak-to-valley height	µm
Re	Reynolds number	-
SF	Solid flux	$kg\ m^{-2}s^{-1}$
T	Temperature	K
u	Gas velocity	m/s
V	Volume	M^3

Greek

α	Wake region	
δ	bubble fraction	-
Ɛ	Porosity	
δ	Membrane thickness	m
ρ	Density	kg/m^3
μ	Viscosity	$kg\ m^{-1}\ s^{-1}$
Ø	Sphericity	-

Subcripts

0	Superficial
2D	Two-dimensional
3D	Three-dimensional

b	Bubble
bc	Bubble-cloud
be	Bubble-emulsion
br	Single bubble rise
bs	Bubble solids
ce	Cloud-emulsion
e	Emulsion phase
g	Gas
mf	Minimum fluidization
mp	Melting point
p	Particle
rf	Steam methane reforming
s	Solid phase
w	Wake
x	Lateral slice
y	Axial slice

Chapter 1 Introduction

Climate change is one of the main challenges for this century as recently discussed in the well-known Paris Agreement. Climate change is mostly associated to the extensive use of fuel sources in power generation and transportation sectors, which release plenty of carbon based emissions. Among possible solutions, the use of renewable sources is the most desired. However, the complete energy system cannot immediately be modified and a smooth transition is expected. To do so, still more research is needed in current technologies using non-renewable fuel sources, like those involving hydrogen production. Hydrogen is becoming an attractive energy carrier alternative since it is clean and environmentally friendly as the main product of combustion is steam.

However, hydrogen is not available naturally and it should be produced through fossil fuels or water electrolysis and, in lower extent, renewable energy. Among different processes to obtain hydrogen, the main pathways refer to natural gas or biogas reforming, gasification of coal and biomass, water electrolysis, water splitting by high temperature heat, photoelectrolysis and biological processes [2].

Large-scale hydrogen production is mostly based on reforming of fossil fuels, although only in the case of ultra-purity, water electrolysis is the preferred strategy (around 5% of the total production)[3]. Nowadays, the main drawback of using fossil fuels is the large amount of CO_2 emitted to the atmosphere, which depends on the technology used and the feedstock selected. According to this, methane is fed due to its high H/C ratio [4]. Autothermal reforming (ATR), partial oxidation, dry reforming and steam methane reforming (SMR) are the principal technologies to obtain hydrogen as of methane [2], [4].

In the steam methane reforming, CH_4 is converted into H_2 in a highly endothermic process on a nickel catalyst, operating with excess of steam to reduce the formation of carbon and temperatures above 800˚C (Equation 1). Two water gas shift reactors (Equation 2) (high and low temperature) and a separation unit (mostly pressure swing adsorption) are required afterwards. In this process the number of steps and CO_2 emissions decrease the system efficiency and make the scale-down uneconomical.

$$CH_4 + H_2O \leftrightarrow CO + 3H_2 \qquad \Delta H^{\circ}_{298K} = 205.9\ kJ\ mol^{-1} \qquad \text{[Ec. 1]}$$

$$CO + H_2O \leftrightarrow CO_2 + H_2 \qquad \Delta H^{\circ}_{298K} = -41.1\ kJ\ mol^{-1} \qquad \text{[Ec. 2]}$$

In order to increase the efficiency of this process, novel technologies have been developed recently. Among different technologies related to production, separation and purification of H_2, membrane reactor (MR) technology is proposed as an appealing alternative to replace conventional processes [5]. It is an innovative and promising technology since it integrates reaction and separation in situ, overcoming equilibrium conversion by shifting the conventional thermodynamic equilibrium due to selective removal of the desire product (H_2 in this case) [5], [6]. Different sort of membrane reactor studies have been proposed in packed bed membrane reactors (PBMR), fluidized bed membrane reactors (FBMR) and micro-structured membrane reactors (MMR). Other advantages are shown in Figure 1.

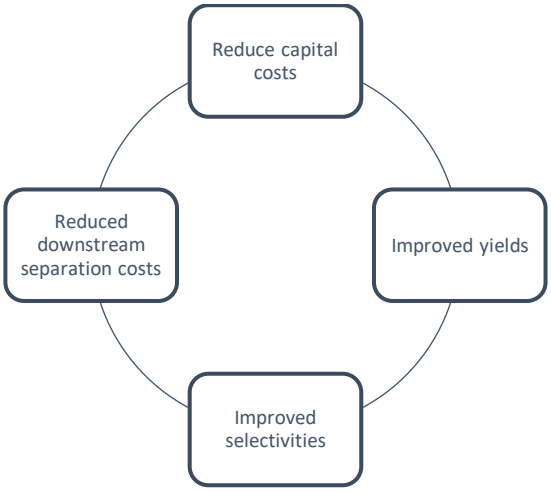

Figure 1. *Advantages of the membrane reactor*

Packed bed configuration has been the most studied one for hydrogen production [7]–[9]. However, it shows many issues which seriously affect the operation and performance. With the recent development of ultra-thin membranes, the rate of hydrogen through the membrane is higher than the transfer from the bulk of the catalytic bed to membrane wall, thus leading to a mass transfer resistance referred to as concentration polarization. Furthermore, the large pressure drop along the reactor determinates the size of catalyst particles. Consequently, mass transfer results a problem and the membrane area must be increased. To achieve a good control of the process it is necessary an exhaustive temperature control on account of possible hot spots which damage the surface of the membrane. On the other side, a decrease of the temperature leads a decrease on the driving force [10].

These problems can be alleviated using a fluidized bed membrane reactor due to the well-mixing between solids and gas providing a good heat and mass transfer ability. Indeed, the rapid mixing leads into virtual isothermal conditions [1].

According to Gallucci et al.[10], the success of membrane reactors for hydrogen production depends on:

- The advances in the membrane fabrication methods for the production of thin membranes with high hydrogen permeances-permeability and perm-selectivity.

- The design of innovate reactor concepts which allow the integration of separation and energy exchange, the reduction of mass and heat transfer resistances and the simplification of the housing and sealing membranes.

In order to make the membrane reactor technology interesting at industrial scale, the following characteristics must be achieved [10]:

i) High selectivity towards hydrogen

ii) High flux

iii) Low cost

iv) High mechanical and chemical stability.

Among this, palladium-based membranes are the most used due to their potential in hydrogen purification. The metal has the potential for the selective removal and separation of hydrogen and can serve in catalytic membrane reactors at high temperature [11].

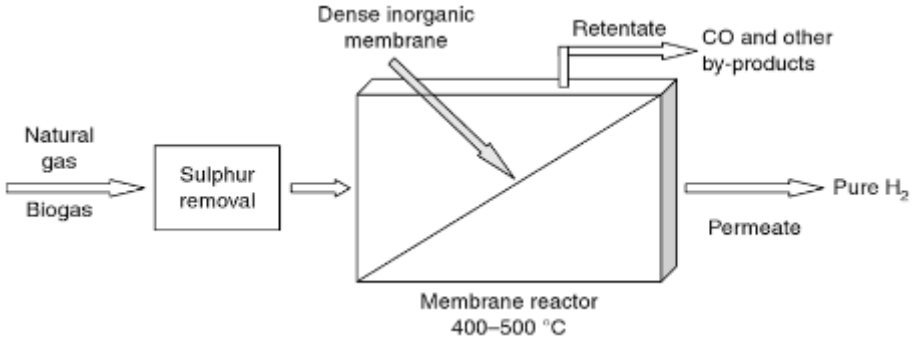

Figure 2. *Palladium membrane operation*

Palladium must be alloyed with another metal because of embrittlement problems, surface poisoning by sulphur compounds [12] and CO [6]. Generally, these metals are silver, gold, nickel and copper [13]. Although Pd-Cu and Pd-Au alloys present a relative resistance to poisoning and high thermal resistance, they show lower permeabilities as compared to Pd-Ag alloys. In an equilibrium, limited system like in steam methane reforming, hydrogen separation from the bed will result in a displacement of the thermodynamic equilibrium, thus achieving higher fuel conversion. However, membrane reactor technology is limited by the operating temperature of the membranes, which is in the range between 600˚C and 250˚C. Higher temperatures would lead into Pd interaction with the support, while at lower temperatures there is Pd embrittlement.

Pd-based membranes can be self-supported (> 50 um thickness). However, they become non-interesting for large scale applications. Therefore, normally the Pd-based membranes are deposited onto porous supports by different techniques such as electroless plating (ELP) and PVD Magnetron Sputtering (PVD-MS) to provide mechanical stability and increased fluxes. Generally, this support could be ceramic or metallic. Ceramic supports are cheaper than metallic and normally show less resistance for gas permeation through them. However, they normally show problems in the sealing due to the lower mechanical strength. On the other hand, metallic supports are more robust and there is no need of sealing if the welding between the porous and dense part is performed [10]. However, they are more expensive and at high temperatures they suffer from metallic interaction between the Pd and the support. To avoid this, an inter-metallic diffusion barrier layer between the metallic support and the metallic selective layer is normally placed [10], [14]. Commonly, this layer could be made of many materials such as ZrO_2 [15], [16], YSZ [17], [18], Al_2O_3 [19], [20], zeolites [21], [22] and graphite [23].

From an economical point of view, membrane costs will be reduced employing a selective membrane which implies less area and less palladium. However, a small pore size, smooth surface and a narrow pore distribution are required, so its cost will increase [10]. This fact aims to the idea of reuse the support, being an important advantage for the company.

In order to make this technology more attractive for industrial scale, an enhancement in the design and scale-up are required. This is done through the use of detailed phenomenological models which

predict the behaviour of fixed and fluidized bed membrane reactor. They assume many correlations and assumptions to solve the hydrodynamics and mass transfer inside the reactor.

Referring to the fluidized bed membrane reactor configuration, the hydrodynamics describe the different phases of the system: the bubble properties along the bed and the movement of solids [1], [24]. Different phenomenological reactor models for gas-solid fluidized bed reactors have been developed [25]–[27]. Most correlations have been obtained at room temperature and without reactive conditions and then, extrapolated to elevated temperatures and with chemical reactions [28], which might lead to wrongly approximations.

As it is possible to find in open literature, different experimental techniques have been used to determinate information from hydrodynamics at room temperature. However, they are focus on emulsion phase or bubble phase. These techniques are classified in invasive and non-invasive techniques which are shown in Figure 3 [29]–[31]

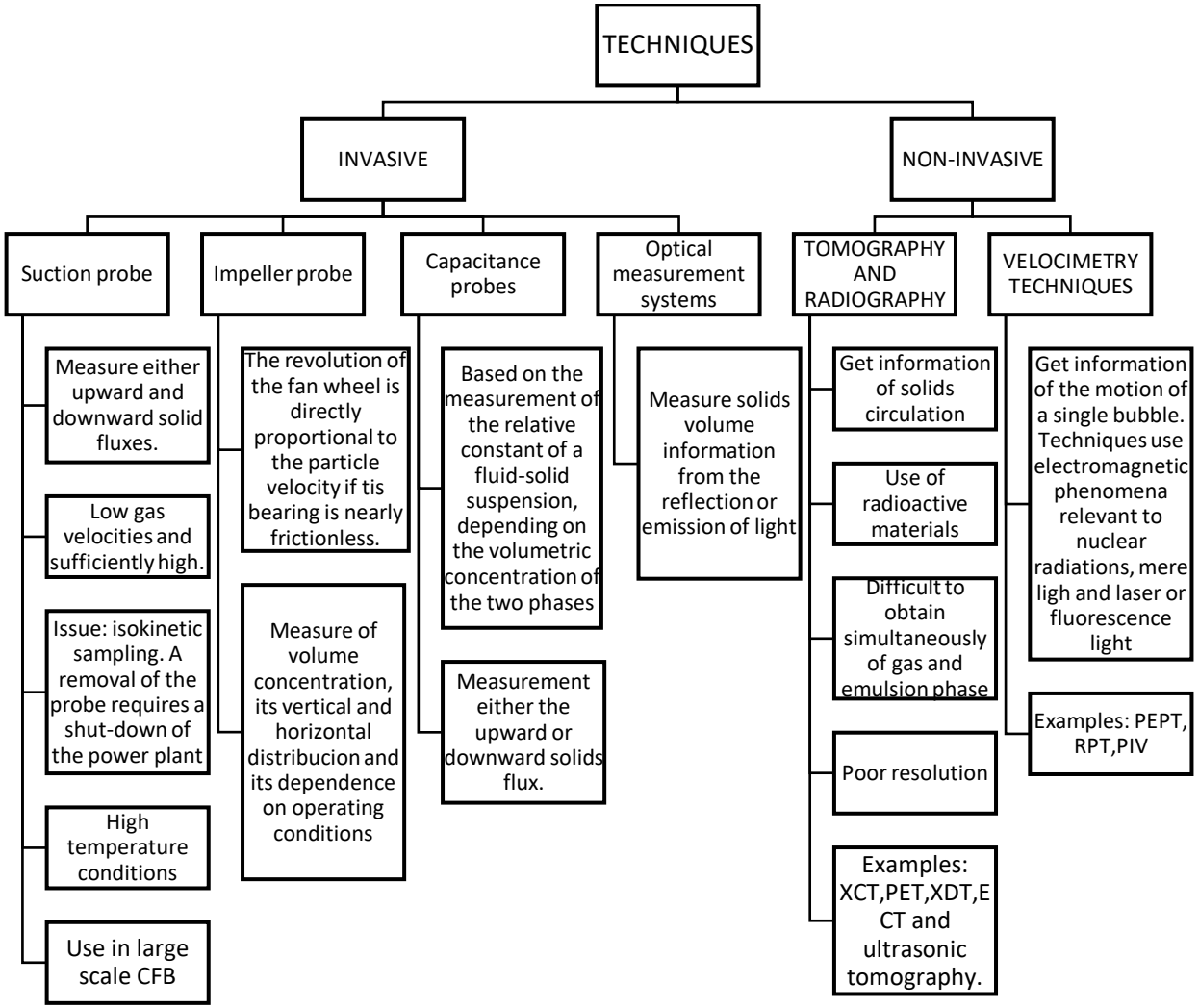

Figure 3. *Experimental techniques for hydrodynamics information*

These methods could be improved thanks to novel techniques, allowing for an enhancement in the accuracy of its assumptions and correlations. Laverman [32], in 2012, proposed a new technique which combines Particle Image Velocimetry (PIV) and Digital Image Analysis (DIA) to obtain the solid flux and its direction. Also, information of bubble phase such as velocity, diameter, bubble fraction or position. As it is reported in literature, PIV/DIA has only been applied at room temperature.

On the other hand, mass transfer is related to the exchange between gas inside bubbles and the gas in the solid phase. As it is represented in Figure 4, mass transfer rates are defined by two summative terms. The convective term refers to the gas through-flow from the bottom of the bubble to the top, especially in large bubbles. The diffusive term is dominated by the molecular diffusion of the gas from the bubbles to the emulsion phase and is more important for small bubbles [24].

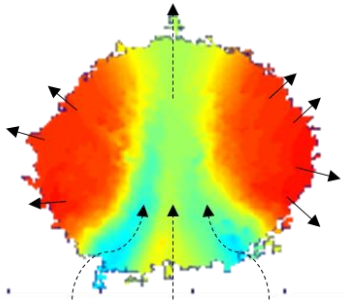

Figure 4. *Bubble to emulsion mass transfer rates: gas convection (dashed) and gas diffusion (line)*

Three approaches have been carrying out to explain the interchange of gas.

First, Zenz and Othmer, Orcutt et al. and Davidson and Harrison, in the early 60's [33], [34], accomplished a theoretical approach where mass exchange occurs due to the combination of force convection through the bubble and molecular diffusion from the bubble to emulsion phases [24], ignoring the presence of the cloud. Then, Rowe et al. [35] improved this definition, in which the cloud and the bubble are consider a single well-mixed phase and molecular diffusion is the mechanism which controls the inter-change [34]. Nowadays, it is still widely accepted for single injected bubbles [24]. Later, Kunni and Levenspiel also suggested a resistance to transfer gas at the cloud boundary, leading a concentration in the cloud phase [34]. Thus, three concentrations are considering: in the cloud (C_c), in the bubble (C_b) and in the emulsion phase (C_e) and two mass transfer coefficients: k_{bc} and k_{ce}. Currently, this is the tree-phase theoretical approach most used in literature for single bubbles, while for freely bubbling beds, other empirical correlations could be found [1].

According to industrial applications, many companies use fluidized bed reactors at high temperatures for biomass gasifiers or polymerization, among others [28].

Some studies have been accomplished to assess the influence of the temperature, concluding that the fluidization behaviour is largely influenced by the operating temperature [28]. Radmanesh et al. [36] reported that axial mixing enhances because of the rise in the temperature using RPT in a silica-sand bubbling reactor. Also, it was mentioned that, at elevated temperatures, attraction forces between particles are weaker leading to a lower upward solids flux [25].

Recently, it has observed that, at high temperature, bubble shape is affected [28]. Above 300 °C, instead of having a kidney shape, they become bigger, with an equivalent diameter larger than 50% of the column diameter, thus leading to slugs formation. Furthermore, working in this conditions, the

emulsion phase moves in a chaotic way. It seems that the heavy particle rain push down the wake of bubbles with a rough particles displacement. As it is reported, it is difficult to make a fair comparison in terms of bubble properties at different temperatures. In order to make phenomenological models more accurate, it would be important to account for this effect. This change in hydrodynamics characteristics also involves the prediction of the minimum fluidization velocity at higher temperatures. For instance, u_{mf} decreases with increasing temperatures for Geldart B particles [37]. Recently, Campos improved the estimation of u_{mf} based on a new correlation to predict ε_{mf} for spherical particles as a function of the temperature and particle properties. The correlation includes the minimum plateau for ε_{mf} for large Archimedes numbers and the temperature effect related to the inter-particle forces and interactions. Moreover, Campos also explained that the effect of temperature in the fluid dynamics of bubbling gas-solids fluidized beds cannot be fully explained by the changes in gas properties. Particle-particle interactions play an important role in high temperature hydrodynamics [38]

Thus, an even more exhaustive study of the phenomena occurring at high temperatures in fluidized beds is required to further understand the behaviour of a fluidized bed at reacting conditions.

1.1 Research goals

In this work, the main objective is to gain more knowledge on the possibilities of membrane reactors for future industrial implementation by investigating two different things closely related in a membrane reactor. The first one related to the behaviour of the membranes, and the second one concerning correlations for hydrodynamics at high temperatures.

An industrial membrane reactor would commonly mount metallic supported membranes since sealing issues are solved and longer life-times can be expected. However, these membranes are expensive, mostly related to the metallic support. However, until now there is no information in the literature concerning the reutilization of these support materials once the membrane becomes deteriorated and should be substituted. Therefore, in this research a metallic supported membrane has been intentionally damaged after long operation, and subsequently the metallic support has been reused and coated with a new layer of Pd-Ag alloy. The objective is, therefore, to investigate whether this reused membrane can provide similar permeation characteristics as the original membrane. This research is of great interest prior the commercialization of membrane technology since metallic supports might represent up to half of the costs of a membrane and its reutilization might lead into important economical saves. In this work, first a long-term membrane stability test has been carried out at different temperatures and the membrane behaviour has been compared to the original membrane. Subsequently, because of the importance for membrane design and process optimization [6], the influence of CO and N_2 is tested. Finally, the performance of this membrane has been tested under reactive conditions for the water gas shift reaction in a fluidized bed membrane reactor using a commercial $Ni/CaAl_2O_4$ catalyst (HiFUEL® R110) provided by Johnson Matthey. The results under reactive conditions are evaluated using a modified three phase model from Kunii and Levenspiel to estimate the sensitivity in membrane characteristics on the performance of the process.

The second investigation in this study is related to the improvement of existing correlations commonly used in phenomenological models describing fluidized bed (membrane) reactors. This research deals with the extension of a recently fundamental research carried out by Mustafa Taşdemir [1] for fluidized beds at room temperature, who developed a correlation to predict solids movement inside fluidized beds as function of bubble properties using novel optical PIV/DIA techniques. In this research, the investigation is extended to high temperature systems using data obtained with the recently

developed High-Temperature PIV by Ildefonso Campos. Therefore, the aim of this research is to investigate the effect of elevated temperatures in both phases at the same time for having a useful correlation, thus allowing a better design of a gas-solid fluidized bed (membrane) reactor.

Chapter 2 Theoretical overview

2.1 Membrane

Membranes are barriers that allow the flow of some components of a feed fluid mixture. The movement (permeation) is caused by a potential force or a driving force between both sides of the membrane. The fluid mixture could be:

- Gas-Liquid
- Liquid-Liquid
- Gas-gas

The stream containing the components that permeate through the membrane is called permeate and the stream containing the retained components is called retentate.

In the case of Pd-Ag based membranes, the mechanism of hydrogen permeation through these dense metal membranes follows a solution-diffusion mechanism. The steps involved in hydrogen transport from a high to a low-pressure gas are represented in Figure 5.

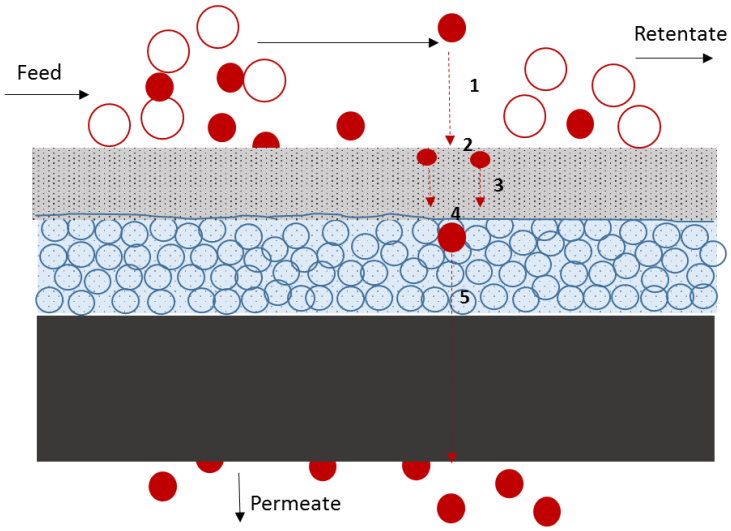

Figure 5. *Mechanism of hydrogen permeation through dense metal membranes*

1. Diffusion of molecular hydrogen to the surface of the metal membrane
2. Reversible dissociative adsorption on the metal surface

3. Diffusion of hydrogen atoms through the metal layer

4. Association of hydrogen atoms on the ceramic surface

5. Diffusion of atomic hydrogen through the ceramic layer and bulk metal

Mass transfer takes place in non-equilibrium systems. This phenomenon has two transport mechanism:

- Diffusion: molecular movement origin because of a gradient, normally density gradient.

- Convection: mass transfer phenomenon caused by a macroscopic fluid movement.

Diffusion can be treated mathematically by Fick's equation (see Ec.3). Permeation H_2 flux, J_{H_2} $[\frac{mol}{m^2*s}]$, follows a solution-diffusion mechanism [39], [40]:

$$J_{H_2} = \frac{L_{H_2}}{\partial}(p^n_{H_2,feed} - p^n_{H_2,permeate}) \qquad \text{[Ec. 3]}$$

Where $L_{H_2}[\frac{mol*m}{m^2*s*Pa^n}]$ is the Pd alloy permeability to H_2, $\partial\ [m]$ is the membrane thickness, $p^n_{H_2,feed}$ and $p^n_{H_2,permeate}\ [Pa^n]$ are the hydrogen partial pressures in the feed side and in the permeate side, respectively, and *n* is the pressure exponent. Pressure exponent value varies between 0.5 and 1. The first one means that the permeation is more limited due to the diffusion of atomic hydrogen control and, the second one, that the slowest step is the dissociation, where the permeation is not restricted [6].

Moreover, permeability follows an Arrhenius-type equation:

$$L_{H_2} = L_{0,H_2} * \exp(-\frac{E_a}{RT}) \qquad \text{[Ec. 4]}$$

Where $L_{0,H_2}[\frac{mol*m}{m^2*s*Pa^n}]$ is the pre-exponential factor and $E_a\ [J/mol]$ is the activation energy values.

Pre-exponential factor, E_a and *n* have been determinate from the linear fit between H_2 permeation flux, J_{H2}, and the pressure drop between the feed and permeation side.

2.2 Fluidized bed reactors

As defined by Kunii and Levenspiel, fluidization is the operation by which solid particles are transformed into a fluid-like state through suspension in a gas or liquid [41]. At low rates, the fluid merely percolates through the void spaces between particles which remain in place. This is known as a packed or fixed bed reactor. With an increase in flow rate, particles move apart and the reactor will achieve a stage in which the pressure drop through any section of the bed equals the weight of particles and fluid in that section. This is known as minimum fluidization.

Above the point of minimum fluidization, instabilities with bubbling and channelling of gas are observed. In other words, agitation becomes more violent and the movement of solids is thoroughly agitated. Increasing the gas velocity leads to different fluidization regimes as it is shown in Figure 5.

Solid particles are typically supported by a porous plate, known as a distributor. The fluid passes through this distributor towards the solid material. Depending on the flow rate, the form of contacting of a batch of solids with the fluid is modified as it is shown in Figure 6 [1].

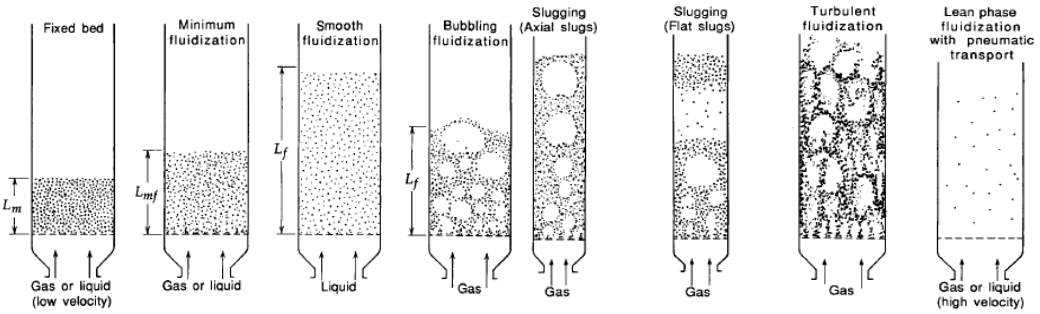

Figure 6. *Forms of contacting of a batch of solids by fluid*

In these reactors, there is a strong interplay between bubble and solid phases, which leads into many advantages of these type of reactors compared to other reactor configurations. However, this also implies some disadvantages. The bubble properties, such as bubble diameter (d_b), bubble rise velocity (u_b) and bubble fraction (δ) depend on the superficial gas velocity, which in turns is responsible of the solids velocity and solids interactions.

Some of the main advantages compared to conventional fixed bed reactors are summarized in the following points:

- Efficient mixing that improves solid-gas contact time leading in a high heat and mass transfer rates between fluidized beds and an immersed object.

- Rapid mixing of solids leading in an isothermal reactor conditions and easier reactor control. Low risk of hot sports, runaway and thermal instability.

- The ability to withdraw and reintroduce solids continuously.

- Possibility to continuous regeneration of the catalyst particles.

In the same way, some disadvantages of fluidized beds are:

- Particle attrition due to the vigorous mixing impacting in the residence time and the possibility to agglomeration with the subsequent bed defluidization and emergency shut-down [28].

- For the same weight of catalyst, expansion of the bed requires an increase in reactor volume

- Scale-up and design presents important challenges which limits the use of these reactors to applications that can justify the significant research and development efforts involved.

Nowadays, thanks to all experimental research carried out in the last decades, it is possible to understand and predict better the behaviour of fluidized beds. Currently, the design of fluidized beds is done through the use of the phenomenological models. In particular, the most often used in the literature is the one developed by Kunii and Levenspiel, which describes better the hydrodynamics and mass transfer of a fluidized beds. The model is based on the Davidson's explanation of the movement of gas around a rising bubble and Rowe's finding on bubble wakes. In the Kunii-Levenspiel model, the reactant gas enters the bottom of the bed and flows up through the reactor in the form of bubbles. As the bubbles rise, mass transfer of the reactant gases takes place as they flow in and out of the bubble to contact the solid particles, where the reaction product is formed. The product then flows back into a bubble and finally exits the bed when the bubble reaches the top of the bed.

A summary of the hydrodynamics and mass transfer correlations is reported in Table 1.

Table 1. *Hydrodinamic and mass transfer correlations in phenomenological model*

Hydrodynamics	
Minimum fluidization velocity [42]	$\frac{Ar}{Re_{mf}} = 150\frac{1-\varepsilon_{mf}}{\emptyset^2\varepsilon_{mf}^3} + 1.75\frac{Re_{mf}}{\emptyset\varepsilon_{mf}^3}$ $Ar = \frac{d_p^3\rho_g(\rho_p-\rho_g)g}{\mu_g^2}$ $Re_{mf} = \frac{\rho_g u_{mf} d_p}{\mu_g}$
Minimum fluidization voidage [43]	$\varepsilon_{mf} = 0.586Ar^{-0.029}(\frac{\rho_g}{\rho_p})^{0.021}$
Bubble diameter [44]	$d_b = d_{b,max} - (d_{b,max} - d_{b,0})e^{\frac{-0.3h}{D_T}}$ $d_{b,max} = 0.65[\frac{\pi}{4D_T^2(u_0-u_{mf})}]^{0.4}$ $d_{b,0} = 2.78/g(u_0-u_{mf})^2$
Bubble velocity [33]	$u_b = u_0 - u_{mf} + 0.711(gd_b)^{1/2}$
Emulsion velocity [45]	$u_{g,e} = \frac{u_0 - (\delta + f_w\varepsilon_{mf})u_b}{f_{ce}\varepsilon_{mf}}$

Bubble fraction [41]	$\delta = \frac{u_0 - u_{mf}}{u_b}$
Wake fraction[46]	$f_w = \alpha\delta$ with $\alpha = 0.15$
Emulsion fraction	$f_{ce} = 1 - (\delta + f_w)$
Mass transfer	
Binary gas diffusion coefficients [41]	$D_{AB} = \frac{10^{-3}T^{1.75}(\frac{1}{M_A} + \frac{1}{M_B})^{0.5}}{P[(\sum V_A)^{\frac{1}{3}} + (\sum V_{AB})^{\frac{1}{3}}]^2}$
Mass transfer coefficients gas phase [41]	$K_{i,bc} = 4.5\left(\frac{u_{mf}}{d_b}\right) + 5.85\left(\frac{D_j^{0.5} g^{0.25}}{d_b^{1.25}}\right)$ $K_{i,ce} = (\frac{\varepsilon_{mf} D_j u_b}{d_b^3})^{0.5}$ $with\ \frac{1}{K_{i,be}} \approx \frac{1}{K_{i,bc}} + \frac{1}{K_{i,ce}}$

Early investigators saw that two phases could be distinguished in fluidized beds: emulsion and bubble phase (often called dense and lean phases). The emulsion is the region of higher density, while the region with bubbles has a low solid density. The region just below the bubble is the *wake region* (α) [41]. Typical bubbles are not spherical but have a flattish or even a concave base. The movement of solids in a fluidized bed is induced by the wake of bubbles [1]. The region penetrated by gas from a rising bubble is called the *cloud,* an intermediate phase between the bubble and the emulsion phases as observed in Figure 7 [47].

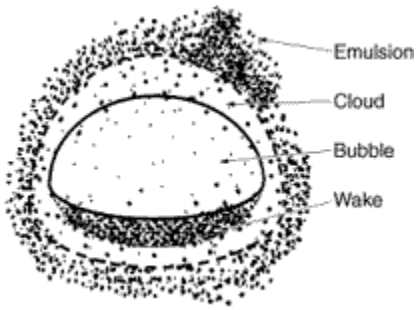

Figure 7. *Schematic of bubble, cloud and wake [69]*

As it is said, the first significant breakthrough was made by Davidson, whose model accounted for the movement of both gas and solids and the pressure distribution about rising bubbles. Then, some alternative analyses have been proposed. Kunii and Levenspiel realized that in some aspects the Davidson model does not fit the data as well as some of other models do. Thus, they developed the model with the follow assumptions [47]:

- The bubbles are all of one size
- Solids in the emulsion phase flow smoothly downward, essentially in plug flow
- The emulsion phase exists at minimum fluidizing conditions
- The void fraction in the wake is equal to the void fraction of the emulsion phase, and the average gas and solid velocity in the wake is assumed to be the same and equal to the upward velocity of the bubbles.

Many assumptions are questionable validity. Some of them are still used in the description of the hydrodynamics of detailed modelling in fluidized bed reactors having no impact on the results. Nevertheless, for alternative cases, these assumptions would have a significant impact. Therefore, Mustafa Taşdemir [1] developed a correlation to predict solids movement inside fluidized beds as function of bubble properties using novel optical PIV/DIA techniques, although limited to room temperature measurements.

2.2.1 Overview of bubble fraction

Bubble fraction, δ, refers to the portion of the bed occupied by bubbles. According to the Kunii-Levenspiel model, the expression for the bubble fraction could be represented simply by the equation 5, which is related to the superficial excess gas velocity:

$$\delta = \frac{u_0 - u_{mf}}{u_b} \qquad \text{[Ec. 5]}$$

Which is valid for $u_b \cong 5\, u_{mf}/\varepsilon_{mf}$.

Mustafa Taşdemir [15] compared this theoretical bubble fraction with experimental findings using the non-intrusive optical technique PIV/DIA. The bubble fraction was determined by taking slices at different axial positions and subsequently dividing instantaneous images into bubble and emulsion

phases throughout the bed. Pixels defined as bubble are divided by the number of pixels contained in the slice, hence giving the bubble fraction on an axial position. Several experiments using glass beads and different excess gases were carried out. Results showed that early theoretical correlations tend to overestimate the bubble fraction in the bed due to the assumptions made in the derivation. Therefore, a new correlation for the bubble fraction was presented based on the obtained experimental data, although valid for spherical particles at room temperature:

$$\delta = 0.24(u_0 - u_{mf})^{0.39} \qquad \text{[Ec. 6]}$$

As it is presented, bubble fraction solely depends on the excess gas velocity and not on parameters such as the particle size or particle density. The novel method can be used on different particles types, but a further investigation at high temperatures is required.

2.2.2 Overview of wake parameter

It is well accepted that the movement of solids in a fluidized bed is induced by the wake of bubbles. It happens since the pressure in the bottom part of the bubble is lower than in the nearby emulsion. Therefore, gas is drawn into the bubble causing a turbulence mixing behind the bubble. Figure 8 shows how rising bubbles drag a wake of solids up the bed behind it, and that the wake sheds solids at it rises [41]. The net flow of the solids in the emulsion phase must therefore be downward. The gas within a particular bubble remains largely within that bubble, penetrating only a short distance into the cloud [47].

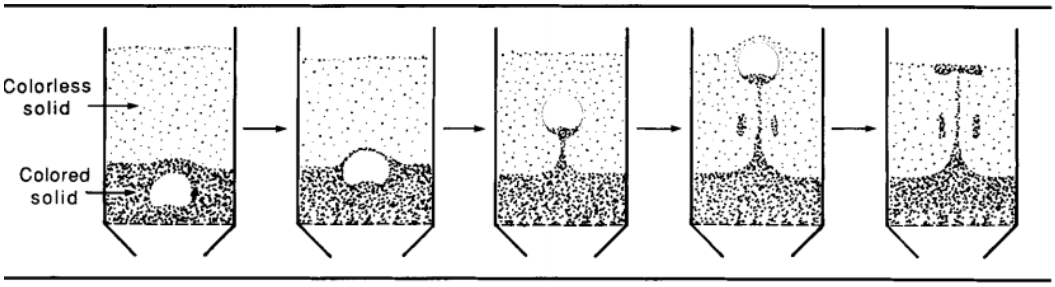

Figure 8. *Sketches of photographs by Rowe and Partridge showing the entrainment of solids by a rising bubble [41].*

When introducing this characteristic behaviour of the wake phase in a phenomenological model, two main assumptions are considered:

- The wake has exactly the same velocity as the bubbles
- The wake fraction is proportionally constant to the bubble fraction in the bed

The first assumption is used to solve the mass balance in fluidized beds. The second one is based on the analysis of the geometry for injected bubbles in an incipient fluidized bed. In these assumptions, the wake is defined based on geometry considering spherical cap bubbles as it is shown in Ec.7

$$\alpha = \frac{V_w}{V_b} \qquad \text{[Ec. 7]}$$

As it has observed, bubbles have an approximately hemispherical top and a pushed-in bottom. M. Tasdemir found that a small change in the definition in the wake fraction has an important effect on the behaviour of reactive conditions limited by gas mass transfer between bubble and emulsion phases. This idea leads to Mustafa Taşdemir to determine wake properties based on solid flux profiles obtained using optical techniques to solve the mass balance inside the fluidized bed. Through the technique, PIV/DIA, it is determined average amount of solids moving upwards in the bed as a function of bubble fraction and bubble properties.

In his novel method, bubble fraction, bubble diameter, bubble rise velocity and solid fluxes are first measured for different conditions. Subsequently, the method combines the average results obtained for solid fluxes and the bubble properties in order to solve the internal mass balance of a fluidized bed. Both images could see in Figure 9.

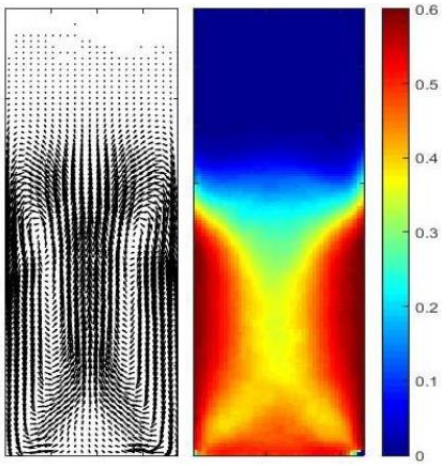

Figure 9. *Average solid velocities in bed from PIV (left) and average bed porosity from DIA(right)*

Solid fluxes obtained experimentally from PIV/DIA and the theoretical solids fluxes from equation 8 should be equal to solve the internal mass balance. Thus, to obtain the theoretical positive volumetric flow, the first assumption has been taken into account. That is, assuming that wake rises with the same velocity as bubble do. The upward volumetric flow is calculated by the following equation:

$$SF_y = \alpha_y * \delta_y * u_{b,y} * \left(1 - \varepsilon_{m,f}\right) * A$$

$$\left(\frac{m_s^3}{s}\right) = \left(\frac{m_w^3}{m_b^3}\right) * \left(\frac{m_b^3}{m_R^3}\right) * \left(\frac{m_R}{s}\right) * \left(\frac{m_s^3}{m_w^3}\right) * m_R^2 \qquad \text{[Ec. 8]}$$

Where α_y is the wake parameter, δ_y is the bubble fraction, $u_{b,y}$ is the bubble velocity rise obtained experimentally, $\varepsilon_{m,f}$ is the void fraction in a bed at minimum fluidization conditions calculated using equation 9 and A_r is the area of the reactor.

$$\varepsilon_{mf} = 0{,}586 * Ar^{-0{,}029} * (\frac{\rho_g}{\rho_p})^{0{,}021} \qquad \text{[Ec. 9]}$$

Different particle types and at different gas velocities were used in order to determine the solid flow and therefore, to determine wake parameter as it is observed in Figure 10.

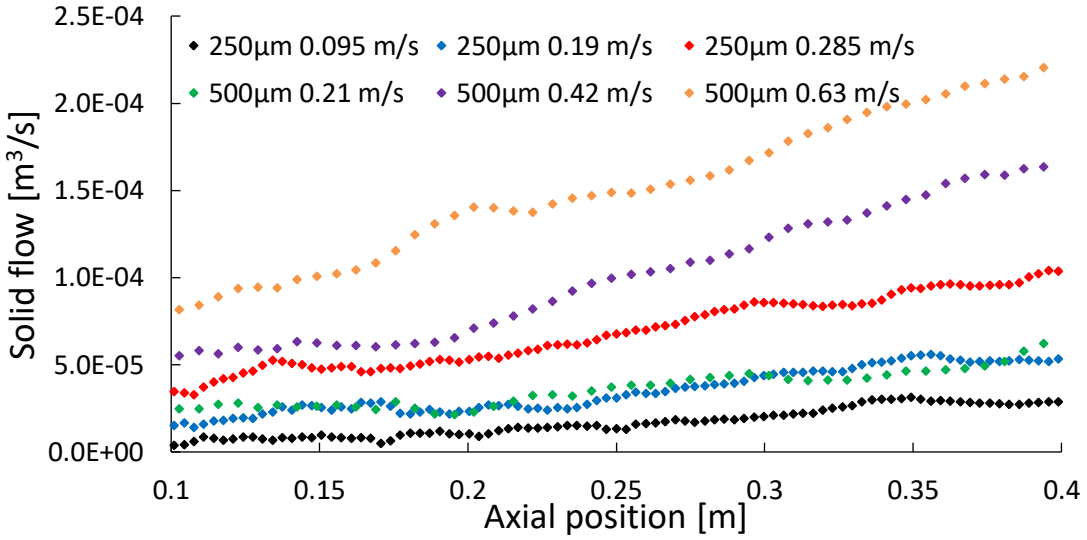

Figure 10. *Solid flows as a function of axial position for glass beads of 250 µm and 500 µm at different excess gas velocities*

The linearly increasing solid flows obtained from PIV/DIA imply that the wake parameter is related to the bubble diameter. Rowe et al. [35] proposed that the shape of the bubbles varies as they grow, thus increasing the wake parameter.

Based on this assumption, a correlation for the wake parameter in 2D fluidized beds was developed. It is based on one of the three relations proposed by Rowe and Widmer [48] for 3D fluidized beds when working outside the range due to it gives reasonable results:

$$\frac{V_b}{V_s} = e^{-0.057*d_b} \qquad \text{[Ec. 10]}$$

So, for 2D bed yields the equation is:

$$\frac{A_b}{A_s} = e^{-0.057*d_b} \qquad \text{[Ec. 11]}$$

Experimental and theoretical solid fluxes were fitted to determinate the coefficient using the squared method.

The form of the relation for the wake parameter can be rewritten as equation 12:

$$\alpha = 1 - e^{M*d_b} \qquad \text{[Ec. 12]}$$

Where M is fitted to a value of -4.92 using the squares method with a R-squared of 0.96. The theoretical solid fluxes calculated with the novel correlation and experimental ones, are plotted in Figure 11.

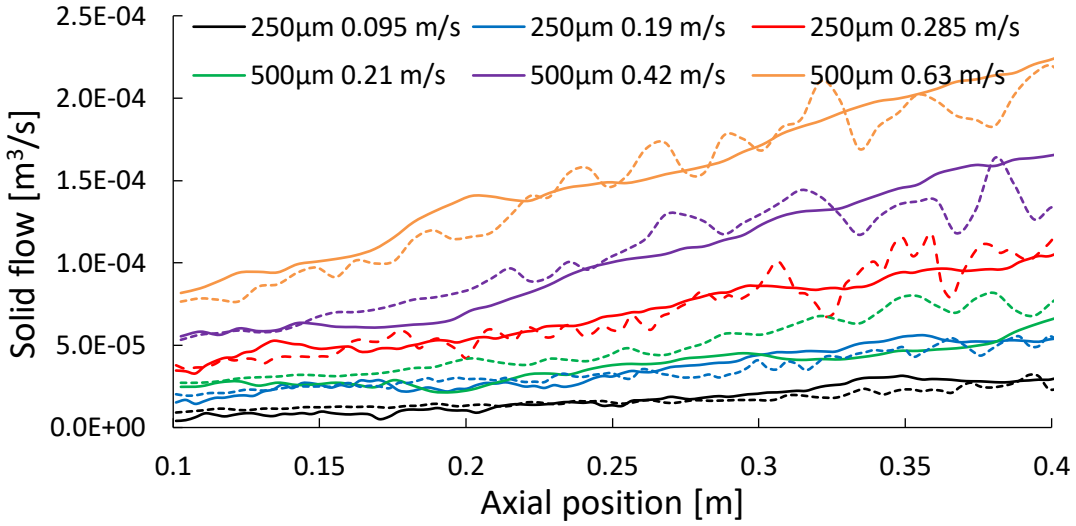

Figure 11. *Solid flows calculated using wake parameter developed by Mustafa (dashed) against solid flows from PIV/DIA (line)*

It can be seen that the new correlation gives a better description of the solid flows than the constant value used for the wake parameter in literature and that it solves the mass balance in the bed.

However, because many industrial processes are carried out at high temperatures, this method should be extended to high temperature systems to further investigate if this assumption is valid. An overall description of the occurring phenomena in fluidized beds at elevated temperature would improve the reactor design, operation and understanding.

Recently, Campos Velarde et al. [28] developed a novel PIV/DIA technique to investigate fluidized bed dynamics at elevated temperatures using a novel endoscopic-laser technique for pseudo-2D columns because of the required visual access. In his work, Campos studied the influence of temperature on the minimum fluidization conditions, developing a new correlation to estimate ε_{mf} for spherical particles (Ec.13) and resulting into a significant improvement in the estimation of U_{mf}.

$$\varepsilon_{mf} = 0.382 * (Ar^{-0.196}\left(\frac{\rho_p}{\rho_g}\right)^{-0.143} + 1)(\frac{T}{T_0})^{0.083} \qquad \text{[Ec. 13]}$$

In this study, the method developed by M. Tasdemir has been applied to experimental data obtained in the recently developed HT-PIV/DIA technique. The main objective is to verify the validity of the correlation at higher temperatures and to, if required, make the correlation temperature dependent.

In the coming section, the experimental techniques and methods are described. Subsequently, the main results are presented and discussed for the membrane testing and the hydrodynamics study. Finally, the work is summarized with the main conclusions and the recommendations for future work.

Chapter 3 Experimental

3.1 Membrane preparation

The metallic supported membrane used in this work was supplied by Tecnalia (Spain). The metallic porous support is made of Hastelloy X (3/8'' o.d.; 0.2 µm media grade) and provided by Mott Corporation after a surface treatment. It consists on grounding and reactivating steps aiming for small pore size and low surface roughness. Finally, this tube is welded to dense Inconel-600 tubes having one closed-end configuration.

In order to avoid inter-metallic diffusion it is deposited a ceramic inter-diffusion layer combining Al_2O_3-YSZ using the deposition technique of powder suspension deposition (PSD) following the procedure described in Pacheco et al. [49]. Once the dip coating process was done, the sample was sintered at 750 ˚C for 2 h. Then, a helium-hydrogen mixture was fed for the cooling step. Subsequently, the electroless plating technique [50] has been used for the deposition of a thin Pd-Ag (~ 5µm) layer on the top of the ceramic barrier. First, the base had a plating process (210 min), followed by a Pd-Ag plating (90 min) in order to increase the membrane thickness and avoid possible pinholes. After each plating step, an annealing treatment was required to alloy the Pd and Ag and eliminate possible undesired compounds. It was carried out at 650 ˚C during 2h by feeding a gas mixture of 10% H_2/90% He. The obtained membrane is shown in Figure 12.

Figure 12. *Metallic supported Pd-Ag membrane*

This membrane has been previously tested at TU/e at intermediate temperatures (400 ^oC) for more than 1200 h showing high permeances and free of defects. In order to prove support reutilization, this membrane was exposed to H_2 at low temperatures, thus resulting in membrane embrittlement to remove the Pd-Ag layer as it can be observed in Figure 1. Subsequently, the membrane was sent back to Tecnalia and a new Pd-Ag layer was deposited on the top of the ceramic layer following the same procedure as for the fresh supported membrane above mentioned.

Figure 13. *Damage metallic supported Pd-Ag membrane*

3.2 Membrane characterization

The aim of this work is to evaluate whether it is possible to reuse the support of a membrane. For this reason, some characterization was carried out to the membrane to check if with a repaired support it has the same characteristics as the initial membrane.

The quality of the ceramic layer has been measured by profilometry [14] to analyse the surface roughness using a Veeco DEKTAK 150 with 2 μm radius stylus tip. The measurements were taken following the standard ISO 4287-4288 (at least 5 measurements and the results are given in Rt). ‘‘Rt”, peak-to-valley height, is the difference between the highest peak and lowest valley in each sample on the evaluated length. Using this technique, it was possible to check whether both membranes were in the same conditions to assess the results.

Once the membrane surface characteristics are assessed, a N_2 leakage check is done with a Bronkhorst flowmeter (model F110C-002; Nominal flow: 0.014-2 Nml/min air) to determine if there is any defect on the surface of the membrane. In order to find where the defects come from, the membrane is immersed in ethanol while helium is fed from inside the membrane.

To performance of the metallic supported membrane (reused), some different tests have been carried out as listed below:

- Long-term single gas permeation tests at high temperature
- Mixed gas membrane permeation tests (influence of CO)
- Test under water gas shift reaction conditions in a fluidized bed reactor

The metallic supported membrane was characterized in a membrane permeation test equipment (see Figure 14) that can be used for testing the permeation properties of the membrane using single gases, simulated mixtures of gases under high temperatures and also in reactive conditions (fluidized and fixed bed configuration). As it is shown in the scheme, the Pd-Ag membrane was surrounded by an external shell which was heated by an oven. In other words, it consists of three sections: feed section, reaction section and analysis section, where in each of them there is a temperature controller. The feed flow rate is controlled by digital mass flow controllers and water by a CEM system (Bronkhorst). The pressure is controlled after the cooler by a pressure regulator.

The reactor is made of stainless steel enclosed in an electric resistance heater. A straight section, 18 cm long, served as a reactor, with a 45 mm inner diameter. A thermocouple placed inside the reactor was connected to a temperature indicator and a temperature controller to monitor and control the reaction temperature.

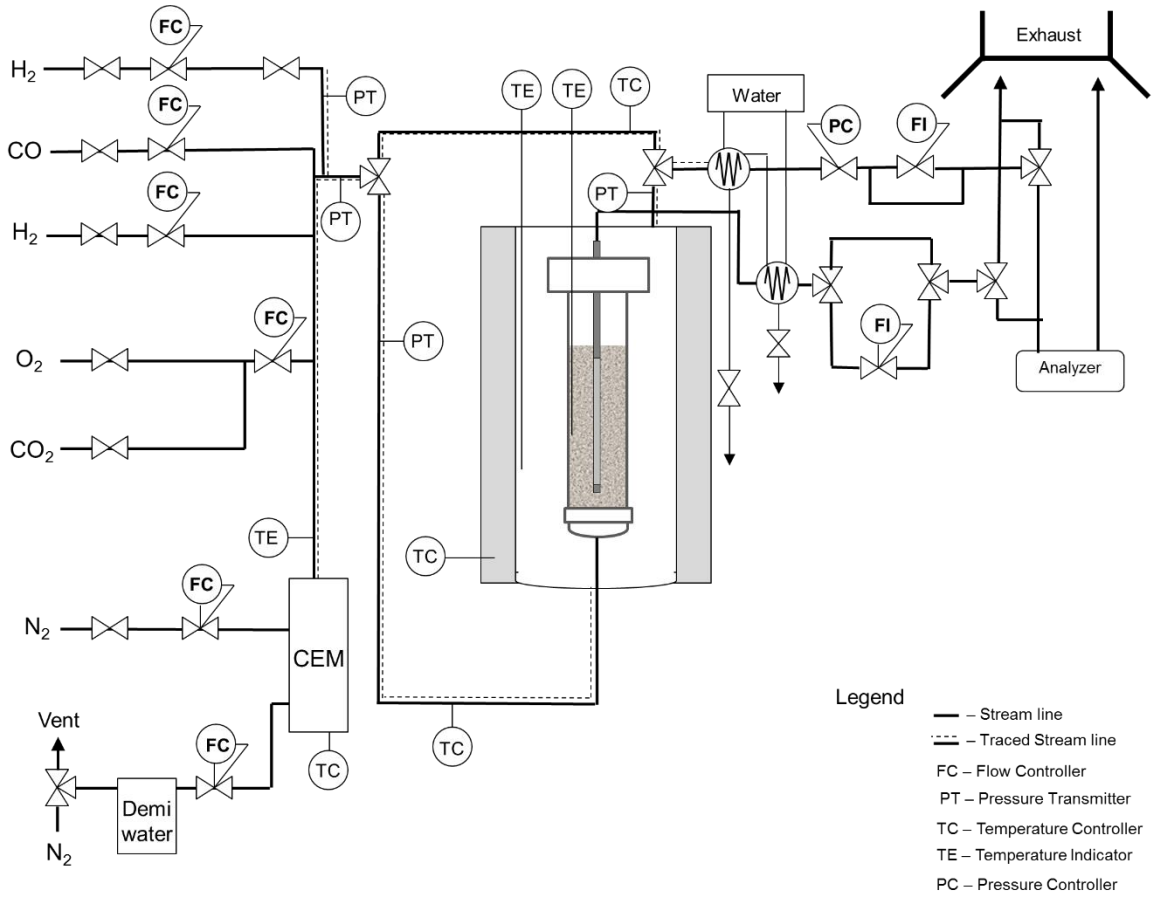

Figure 14. *PFD of reformer setup used for membrane test*

3.2.1 Long-term single gas permeation test at high temperatures

Because the membrane is going to work at high temperatures, it is important to evaluate its stability under harsh conditions as a function of time on stream. This means to check the hydrogen permeation and ideal perm-selectivity as a function of time.

First, the reactor is heated up with a heating rate of 2˚C/min in a N_2 atmosphere and 1 bar until the desired temperature is achieved. Once at high temperature, the feed gas is switched to hydrogen to evaluate the performance of the membrane. In total, it has been exposed to high temperatures during 700 h with a stepwise increase in temperature of 25˚C each week at a constant pressure of 4 bar. Every day, H_2 and N_2 permeance has been measured in order to assess the ideal H_2/N_2 permselectivity as a function of time on stream.

The H_2 and N_2 permeations have been measured using Horibastec film flow meters that allow different flow ranges.

Moreover, to obtain the main parameters of the membrane, a hydrogen permeation test has been performanced at different pressures (1.2-4 bar) for each different temperature (400-500 ˚C) with a constant H_2 feed flow rate of 2 L/min and the permeate side kept at atmospheric pressure.

3.2.2 Mixed gas membrane permeation test (influence of CO)

CO gets adsorbed in the Pd layer acting as a poison since it is responsible of the decrease in the surface area available for H_2 permeation, thus leading into a decrease in H_2 permeation. Therefore, the poisoning effect of CO should be quantified, especially if the membrane is exposed to reforming or shift conditions. This study is carried out by fixing the partial pressure of H_2 at the feeding side, concretely, 3 bar and, at different temperatures and varying the H_2/N_2 and H_2/CO mixtures (5-15 %v/v) correcting for the total inlet pressure. In these experiments the permeation composition was measured with a micro gas chromatograph (GC, Varian CP-4900) to check the impurities in the permeate side.

3.2.3 Water Gas Shift

After single gas tests, the performance of the membrane is also studied under reaction conditions by feeding different semi-industrial WGS feed compositions at different temperatures. Table 2 illustrates the operating window in which the experiments were performed. Steam-carbon ratios used are high enough to neglect carbon formation according to Rostrup-Nielsen [51].

Table 2. Overview of the operating window for the experiments

Pressure [bar]	**4**
u/u_{mf}	3
u_{mf} [m/s]	0,02
CO [%]	10
Temperature [˚C]	400-450
Steam/Carbon	2-2,5-3
Reactors	FBR - FBMR
Catalyst	250 g of $Ni/CaAl_2O_4$

The schematic diagram of the experimental equipment used is given in Figure 14. The feed section contains gas supplied for CO and N_2. Deionized water was delivered by a piston pump to the evaporator where it vaporized into steam and was mixed with the other gases in the different ratios shown in Figure 14. After condensation of the steam and drying of the gas mixture, the effluent was sent to the analysis section. The GC was used to analyze the outlet gases, CH_4, N_2, CO, CO_2 and H_2. The amount of steam was determinate by a hydrogen and oxygen balance.

The reactor was filled with 250 g of a commercial $Ni/CaAl_2O_4$ catalyst provided by Johnson Matthey with a particle size ranging around 150 and 250 mm, with the membrane completely immersed in the bed. In a previous work Medrano et al. [52] studied the attrition of this catalyst and they observed that the particle size distribution does not change neither after 24h of cold fluidization nor 24h of fluidization at 600˚C. Minimum fluidization velocity of the solids phase has been selected according to other previous works at a value of 0.02 m/s at a range of temperatures (350-450˚C) with N_2.

Before and after each experiment, H_2 and N_2 permeance are measured to evaluate if the membrane deteriorates by comparison with the results obtained in the single gas without the catalyst bed for the

same conditions. Thus, also a possible interaction between the surface of the membrane and the catalyst is analyzed [52].

Data results obtained experimentally were compared with the three phase's model from Kunii and Levenspiel applied to a membrane reactor. Through this model, it is possible to describe the gas and solid behaviour in the bed together with kinetics to describe the reaction systems.

3.3 Hydrodynamics study

3.3.1 The PIV/DIA method

Particle Image Velocimetry (PIV) is an optical non-invasive technique that was initially used to investigate fluid dynamics of liquid or gas-liquid systems. However, over last years, it has been adjusted to study the hydrodynamics of fluidized beds [53], [54]. PIV consists of taking consecutive images with a short inter-frame time with a CCD camera. Subsequently, each recorded image is divided into N x N interrogation areas and the use of spatial cross-correlation techniques on two consecutive images to obtain the instantaneous emulsion phase velocity [1]. In this work, images are processed using the commercial software DAVIS. A multi-pass algorithm combined with a 50% overlap of the interrogation areas is used to reconstruct the instantaneous velocity vectors over the whole field of measurement [28].

Laverman et al. coupled PIV with Digital Image Analysis technique (DIA) to estimate simultaneously the solids circulation patterns and bubble properties with high spatial and temporal resolution under cold-flow conditions. DIA is an image post-processing technique capable to distinguish between bubble and emulsion phases according to the pixel intensity.

The algorithm starts by correcting inhomogeneous illumination and lens effects in the images. To do so, a pixel intensity normalization, called background, is done by averaging the intensity of all the frames from an experiment, in which only the pixel intensities of the emulsion phase are taken into account. Image intensity is subsequently normalized within a range between 0 and 1 by subtracting the average background image, assigning 0 to the lowest intensity on the bubble phase and 1 to the emulsion phase. By using a threshold value (0.2 in this work), all connected pixels below this threshold are designated as bubble phase, while if it is beyond it, the pixel is designated as an emulsion phase. Through a correlation proposed by Jong et al. [55] (Equation 14) 2D porosity (or solids fraction) is converted into 3D in a 0-0.6 range to fit with PIV image.

$$\varepsilon_{s,3D} = \begin{cases} \varepsilon_{s,3D,max} & for\ \varepsilon_{s,3D} \geq \varepsilon_{s,3D,max} \\ 1 - \dfrac{1}{B}\varepsilon_{s,2D} & for\ \varepsilon_{s,3D} \leq \varepsilon_{s,3D,max} \end{cases} \qquad \text{[Ec. 14]}$$

Then, DIA is capable of calculating the displacement of the centre of mass of bubbles and bubble properties such as equivalent bubble diameter, position and bubble rise velocity.

Applying PIV/DIA it is possible to measure the average solid fluxes at every axial position over the bed as it is shown in Figure 15. Thus, taking slices throughout the axial position and combining the averages calculated, the lateral solid fluxes per axial slice can be obtained using the following equation:

$$SF_{y,x} = u_{e,y,x} * \varepsilon_{s,y,x} * \rho_s = \frac{px}{time} \times \frac{solids}{reactor\ volume} \times \frac{reactor\ width}{px} \quad \text{[Ec. 15]}$$

$$[\frac{kg}{s \cdot m^2}] = [\frac{m}{s}] \times [\frac{kg}{m^3}]$$

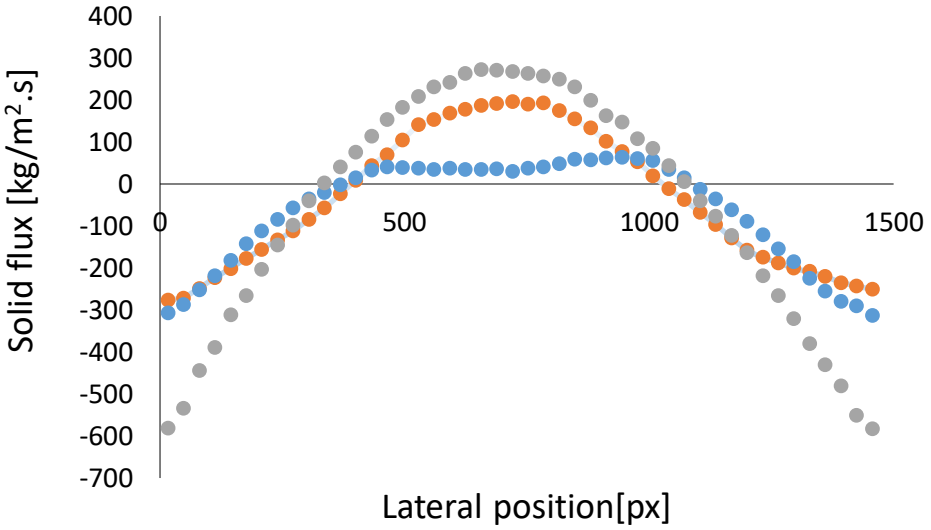

Figure 15. *Solid fluxes in bed at different heights*

Recordings in this work are done with an inter-frame time of 1 ms with a frequency of 2 Hz. The size of the interrogation area could be 256x256 or 128x128 pixels, depending on the image resolution.

3.3.2 PIV/DIA set-up

As previously mentioned, the aim of this research is to extend the recently correlation obtained by Mustafa Taşdemir [1] at room temperature conditions to higher temperature. To do so, data results obtained by Ildefonso Campos with his recently developed High-Temperature PIV technique have been used. In his research, Campos first assessed the validity of the high temperature PIV by comparison with results obtained with a standard PIV/DIA technique using LED illumination (hereafter indicated as LED-PIV/DIA), concluding that the optical endoscope and the high power laser were capable to extend the PIV/DIA technique to elevated temperatures due to good agreement in terms of particle velocity and solids mass flux profiles, as well as the estimation of the equivalent bubble diameter.

For LED-PIV/DIA experiments a “Dantec system Flowsense EO 16M” camera which provides a maximum resolution of 4300x3200 pixels has been used for PIV technique, aligned perpendicularly to the column. Experiments are recorded with a frame rate of 2 Hz in double exposure mode. Particle resolution has been fixed at 2.5 pixels per particle in order to work optimally. A schematic drawing of the setup is presented in Figure 16, where LED lights are placed throughout the bed at different heights to provide a homogeneous illumination.

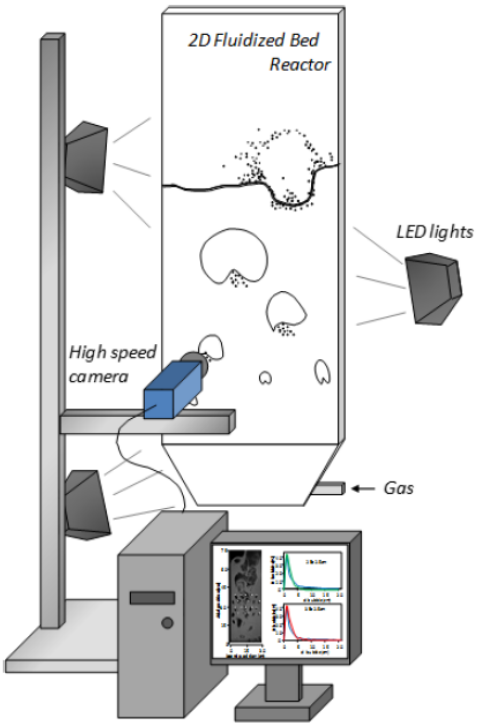

Figure 16. *Experimental LED-PIV/DIA set up*

For the LED-PIV/DIA technique a pseudo 2D column is used with the front wall made of glass, whose sizes are summarized in Table 3. The back wall of the reactor is made of anodized black aluminium to enhance the optical detection of the particles.

Table 3. *Comparsion of LED-PIV/DIA and ePIV/DIA set-up*

Characteristic	***LED- PIV/DIA***	***ePIV/DIA***
Height, width, depth reactor [m]	1.5-0.3-0.015	0.9-0.25-0.015
Recorded area above porous plate [m]	0.1-0.4	0.15-0.4
Porous plate distributor [µm]	40	40
Type of light	LED	Laser
Oven	-	Yes

In the HT-PIV/DIA technique it is necessary to use an endoscope similar to the one depicted in Figure 17 to obtain optical access inside the oven. The one used by Ildefonso [28] is a 38 mm double jacket endoscope manufactured by CesycoKinoptic Endoscopy and supplied by Opto Precision GmbH. The length of the optical endoscope is 940 mm. The lens mounted in the double jacket has a diameter of 18mm while the tip lens inside is 16 mm. Furthermore, a flow of air is fed to the endoscope jacket to

provide thermal protection and to avoid dust deposition. To protect the rest of the endoscope, water is fed through the cooling jacket.

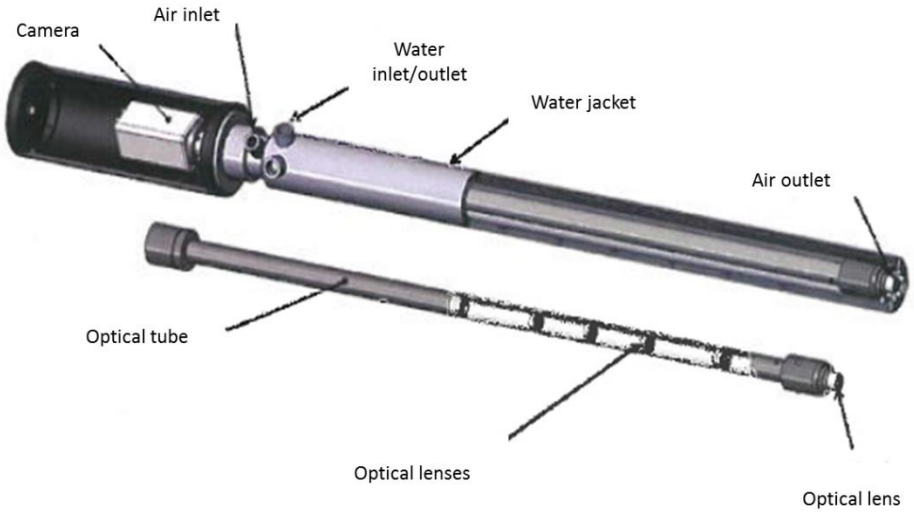

Figure 17. *High-temperature optical endoscope [thesis Ildefonso]*

A pseudo-2D quartz column quite similar to the one used in LED-PIV/DIA experiments is used and placed inside an industrial electrical furnace capable to operate up to 1000 °C (N660 Nabertherm) equipped with an inert sweep gas system. The column is placed inside the high-temperature furnace to provide homogeneous heating and to protect it from heat losses [28]. The distributor chamber and the freeboard of the column are made of Inconel. An Inconel heater is connected to the gas inlet to assure the fed gas enters the fluidized bed at the same temperature as the furnace.

While in LED-PIV/DIA experiments high-speed camera can be placed wherever it fits better, on the other hand, in ePIV/DIA experiments, it must be outside of the furnace. Therefore, the front door of the furnace is supplied with holes in order to insert the two high temperature endoscopes (camera and laser) as it is in the picture below.

Figure 18. *Experimental HT-ePIV/DIA set up. Internal chamber of the furnance (left): optical and laser endoscope inserted through the front door* [28]

The optical endoscope is coupled with the same type of camera as it is used in LED-PIV/DIA experiments which is located outside of the furnace. Illumination is provided by the Nd:Yag double pulse laser Evergreen 70mJ coupled with custom made high temperature endoscope. The illumination system is mounted over a rail system to guarantee good alignment between the laser and the homogenizer. Regarding safety, a nitrogen flush system is included for emergency shut down and/or a quick purge of the fluidized bed [28].

LED lights provide a homogeneous light throughout the bed. However, it becomes more difficult to obtain homogeneous illumination with the laser since it is not placed perpendicular to the column but from a certain angle (see Figure 7), thus leading to a weaker illumination at the top and bottom right corners. Therefore, to estimate the solids hold-up, DIA uses a more robust pixel intensity normalization. For the interrogation area, ePIV/DIA experiments have a 64x64 size, as long as LED-PV/DIA uses a smaller one, 32x32. Laser emits light through pulses, being differences in coherency between each pulse. Once the beam passes through the optics, these differences become bigger, creating intensity spots on fluidized bed surface.

In the next section, first the experimental results obtained with the membrane are presented and compared with the phenomenological model. Subsequently, the comparison between room temperature and high temperature experiments using the PIV/DIA techniques is also presented in order to obtain better correlations that can be implemented in the phenomenological models describing the behaviour of fluidized bed (membrane) reactors.

Chapter 4 Results and discussion

4.1 Membrane characterization

4.1.1 Long-term single gas permeation test at high temperatures

Stability of the repaired membrane has been checked over 700 hours at temperatures ranging between 400˚C and 500 ˚C. The target of this test is to assess the stability of H_2 permeance through the membrane as a function of time on stream and calculate the ideal perm-selectivity by measuring the nitrogen leakage as a function of time and comparison to the original membrane.

The original membrane was exposed at intermediate temperatures (400 ^{o}C) for 1200 h. After the long term test, it was cooled down while feeding H_2 to provoke embrittlement and subsequently, heated up to 400 °C inside the reactor. The results presented in Figure 19 show a good stability for hydrogen permeance during the experiment ($9 \cdot 10^{-7}$ mol·m^{-2}·s^{-1}·Pa^{-1}) as well as an outstanding perm-ideal selectivity (>120000). After cooling down, the ideal perm-selectivity to hydrogen is clearly decreased associated to an increase in N_2 permeation. The significant decrease is related to the embrittlement of the Pd-Ag layer.

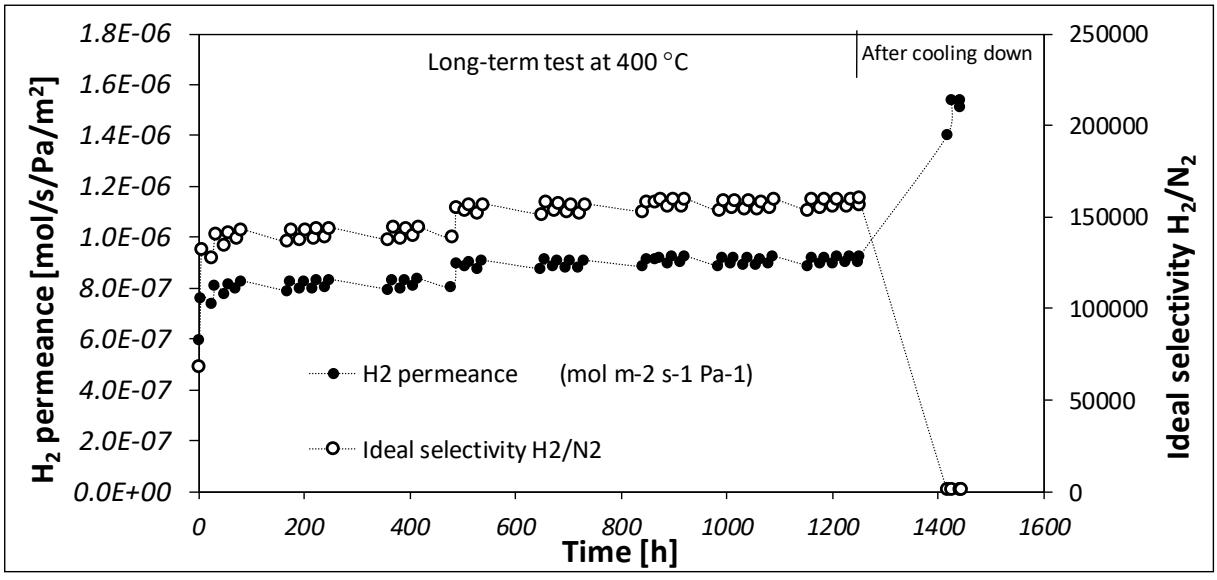

Figure 19. *H_2 permeance (open circles) and H_2/N_2 ideal permselectivity (filled circles) of the original membrane as a function of time at 400˚C*

When comparing these permeation results with the obtained results using the repaired membrane (Figure 20), it is observed a much lower selectivity over time and a lower H_2 permeances for the same

experimental conditions. These observations might be explained by the plating procedure and the possible sintering of the ceramic layer and the metallic porous support. However, at this moment it is not possible to get a detailed explanation about the potential defects on the membrane because first it should be cut for further SEM investigation.

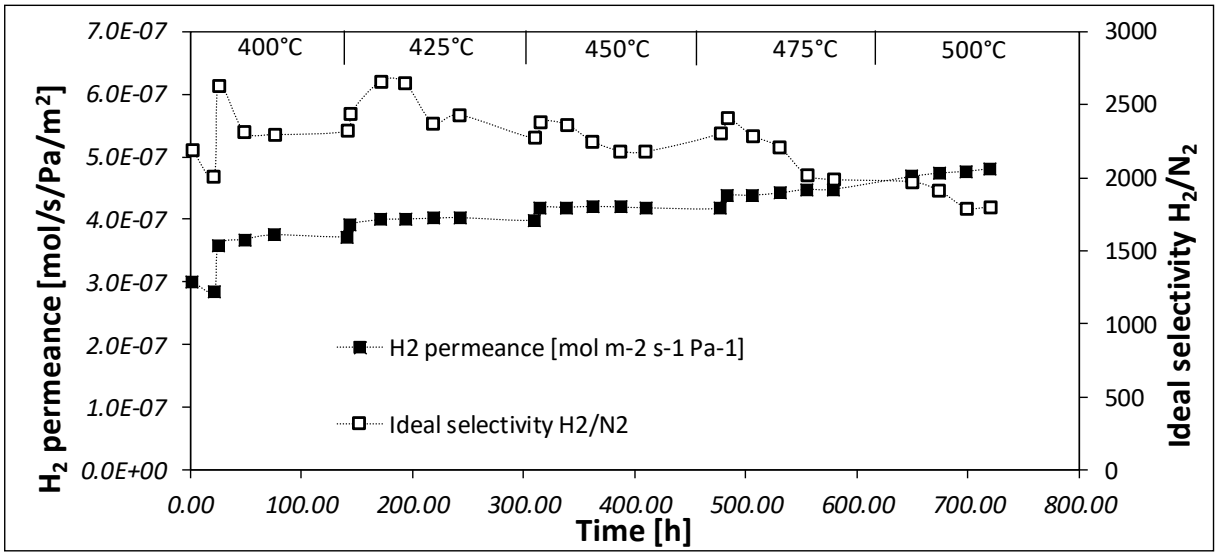

Figure 20. *H_2 permeance (open squares) and H_2/N_2 ideal permselectivity (filled squares) of the metallic supported membrane as a function of time at 400-500˚C*

During this period, the H_2 permeance measured ($4.21 \cdot 10^{-7}$ mol·m^{-2}·s^{-1}·Pa^{-1}) is lower than the one measured for the fresh membrane, as well as the ideal-permselectivity (2248.62). Nevertheless, comparing these values to other metallic supported membranes mentioned in Ref. [14], they are still relatively high as it is summarized in Table 4.

Table 4. Comparison of different Pd based membranes reported in literature

Membrane material (method)	**Selective layer thickness [µm]**	**Support**	**Interdiffusion barrier layer (method)**	**T [˚C]**	**H_2 permeance (10^{-9} [mol m^{-2}s^{-1}Pa^{-1}])**	**Ideal selectivity**	**Refs.**
Pd (PVD+EP)	10-12	Fe-Cr alloy	YSZ (PSD,50 µm thick)	400	112	400-4000 (H_2/N_2)	[56]
Pd (ELP)	20	SS3 16L	Fe-Cr oxide (oxidation)	390	43	200-300 (H_2/N_2)	[57]
Pd-Au (ELP)	2-3	Al_2O_3	NA	500	620	1400 (H_2/N_2)	[58]
Pd-Ag (ELP)	~4-5	Hast X fresh	YSZ-Al_2O_3/YSZ (1 µm thick)	550	1300	>200000 (H_2/N_2)	[52]
Pd-Ag (ELP)	~4-5	Hast X fresh	YSZ-Al_2O_3/YSZ (unknown)	400	900	>120000 (H_2/N_2)	[Previous work
Pd-Ag (ELP)	~4-5	Hast X repaired	YSZ-Al_2O_3/YSZ (unknown)	450	421	2248,62 (H_2/N_2)	[This work]

The fact that the permeance has decreased could be associated to some changes in the ceramic layer as well as in the metallic support. As it is said in the experimental part, Tecnalia did some test during the ceramic layer deposition, whose values of N_2 permeance and roughness before and after the coatings are depicted in Table 5.

Table 5. N_2 permeance and roughness of both membranes before and after the ceramic coatings

Type of support	*N_2 permeance (10^{-9} [mol $m^{-2}s^{-1}Pa^{-1}$])*	*Rt (µm)*
Fresh support	1.426E-05	5.13 – 5.98
Fresh support (with ceramic layer)	8.495E-06	3.86 – 4.76
Fresh support delaminated	2.544E-06	5.41-8.49
Repaired support (with ceramic layer)	2.035E-06	3.09-4.62

According to the table above, N_2 permeance for the fresh support is higher than the membrane with the ceramic layer. As it is known, the thickness of the ceramic layer affects in the permeance, decreasing while the layer becomes thicker. Furthermore, during the different coatings for the depositing of the ceramic layer, the metallic support is exposed to 750 and 800 °C, thus close to the Tamman temperature (around 1/2 and 2/3 of the melting point) of some metals of the alloy such as chromium (T_{mp}=1907 °C), nickel (T_{mp}=1455 °C) or iron (T_{mp}=1538 °C). Therefore, a decrease in the permeance of the membrane could be caused by the thickness of the ceramic layer and the sintering effect in the support. After the stability test with the original membrane, the fresh support was delaminated and its N_2 permeance is lower than in the beginning. This is remarkable, especially because during the delamination part of the ceramic barrier is removed as revealed by XPS analysis. Therefore, it would be expected an increase in the N_2 permeance compared to the fresh support with the ceramic layer. It might be possible that molecules started to move by diffusion for being long under high temperatures, leading in a slight sintering effect. Furthermore, because of the sintering, the pore size of the ceramic layer of the repaired support could be quite smaller, hindering N_2 permeance.

Related to the roughness, Rt value of the delaminated support is higher than the fresh support, thus indicating that part of the ceramic layer of the first membrane remained in the metallic support, as Tecnalia affirmed. To achieve a similar roughness before the plating, several coatings of ceramic layer were carried out until Rt had a value similar to the original membrane with the ceramic layer as can be observed from the results in Table 5. The fact that more coatings were required to achieve the same roughness implied an increase in the thickness of the ceramic layer and, consequently, thicker than the ceramic layer of the fresh support. Therefore, lower permeances were expected.

Membrane characteristics were also evaluated as a function of temperature and pressure and they were compared to the previous membrane. The obtained results are depicted in Table 6. Inspecting the results, permeability is the only parameter that differs from both supports, confirming that the membrane quality has changed. As it is said before, because no SEM test has been done, it is no possible to provide a deeper explanation. Less amount of silver could also be responsible of the decrease in H_2 permeance, although the sintering of the original ceramic barrier is considered the most probable cause. Both metallic membranes tend to have the same mechanism of solution-diffusion through the membrane due to the same value of activation energy and pressure exponent.

Table 6. Comparation of the characteristics of both membranes

Parameter	***Fresh***	***Repaired***
H_2 permeance, J_{H2} [mol $m^{-2}s^{-1}$ Pa^{-n}]	9E-07	4,05E-07
Permselectivity (H_2/N_2)	>120000	2242,47
Ea [kJ/mol]	5,89	5,89
Permeability, $L_{0, H2}$ [mol m^{-1} s^{-1} Pa^{-n}]	4,24E-10	2,04E-10
n	0,738	0,738

4.1.2 Mixed gas permeation tests results (influence of CO dilution)

After studying the stability of the membrane, a permeation test feeding CO and N_2 with H_2 has been carried out at different temperatures (400, 450, 500°C) and pressures. The partial pressure of H_2 has been kept constant (3 bar) for a properly evaluation of the results, while it has been changed the partial pressure of both CO and N_2 depending on the percentage fed. Moreover, all experiments have been done at atmospheric pressure in the permeate side.

As it is depicted in Figure 21 , H_2 partial pressure is kept at 3 bar, which corresponds to the permeance for single gas tests with pure H_2. When giving a closer look at the results, or all cases the H_2 permeance decreases when N_2 (or CO) is fed, thus coming to the conclusion that the other gas creates a mass transfer resistance. The higher the partial pressure of N_2 or CO, the lower the H_2 permeance for all temperatures studied. The decreasing in permeation fluxes is because of the bulk to membrane mass transfer resistances [59]. Nitrogen does not act as a poison, so it does not interact with the surface of the membrane hindering the mass transfer. In case of feeding CO, for all cases, it has a poisoning effect on the performance of the membranes due to its co/adsorption on the metallic surface as it is described in other works [6], [52], [60]. The surface is slowly filling of CO, blocking H_2 flux through the membrane.

As it is reported by other authors [6], [60] for this sort of membranes, there is a significant effect of CO at low concentrations and temperatures. In this case, H_2 permeation decreases quickly because of surface effects. Nevertheless, as the CO content increases, permeation decreases smoothly due to dilution effects, and remaining constant at a certain CO concentration in the inlet steam. It is evidenced in this work, where H_2 permeance slightly decreases for a CO content of 10 and 15%. Also, Figure 21 puts into evidence that higher permeance is found while the temperature increases, in line with other findings in the open literature, in which the poisoning effect of CO was decreased at higher temperatures [59].

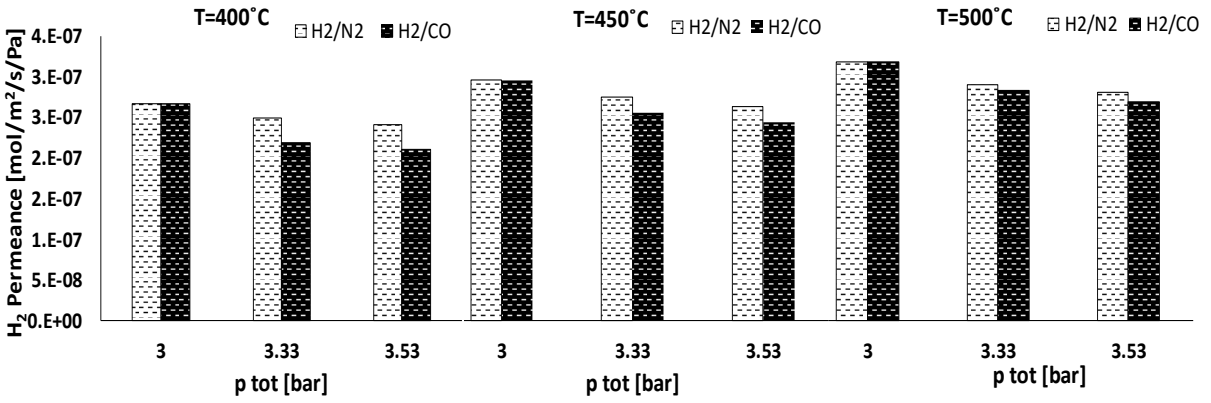

Figure 21. *H_2 permeance as a function of partial pressure of N_2 (white dotted bars) and CO (black dotted bars) at different temperatures*

During the test the H_2 purity in the permeate stream was monitored. For the cases where CO was also fed, CO traces were not observed in the permeate side, but just hydrogen and methane, with a permeate purity of 99.9%. Medrano et al. [52] stated that methanation occurs on the surface of the support forming CH_4 since the support material (Inconel) contains mainly Ni. Thus, this effect may be advantageous for applications in which ultra-pure H_2 is required due to CH_4 has no considerable influence as opposed to CO.

4.1.3 Water Gas Shift

The performance of the membrane is studied at different operating conditions in two different reactors (FBR and FBMR), maintaining a constant pressure of 4 bar in the retentate side and the excess velocity to have similar hydrodynamic conditions in the reactor. This ratio is one of the key parameters that determines the membrane reactor performance. The increase of the inlet rate will result in a lower ratio, leading in a lower hydrogen recovery factor [59]. Experiments were carried out at different temperatures ranging between 400 and 450°C for different amounts of steam and nitrogen, changing the relation S/C.

There is a valve in the outlet of the membrane, allowing the change in the reactor configuration, fluidized bed with internals (FBR) or fluidized bed membrane reactor (FBMR). In the first case, the membrane is immersed but no gas is extracted through the membrane. However, in FBMR, there is H_2 extraction through the membrane [59]. These conditions are sum up in Table 2.

Prior to the experiments, N_2 permeation through the membrane is checked at room temperature and at 4 bar of pressure. Then, catalyst particles are fed followed by the heat-up process described in the experimental section. During experiments, H_2 permeance is monitored under fluidization conditions at different temperatures to check the stability over time by comparison with N_2 permeation to verify that the membrane surface remains at the same conditions [45].

As illustrated in Table 7, the membrane presented a constant behaviour in terms of H_2 permeance during the whole set of experiments. However, the ideal perm-selectivity slightly decreased associated to some surface defects occurring in the membrane. However, without a technique application is not possible to affirm the cause. It might be associated to small defects created in the surface as a consequence of interaction of the Pd-Ag layer with the metallic support [52]. Also, it could be that

there is not a well Pd-Ag layer deposition, being a hole in the membrane or that there are some weak points on the surface due to a defect in the ceramic layer.

Table 7. Properties of the permeate side at different times during WGS study

	T = 400˚C		T = 450˚C	
Parameter	**Before WGS reaction**	**After WGS reaction**	**Before WGS reaction**	**After WGS reaction**
H_2 permeation [$mol \cdot m^{-2} \cdot s^{-1} \cdot Pa^{-1}$]	$4 \cdot 10^{-7}$	$3.9 \cdot 10^{-7}$	$4.4 \cdot 10^{-7}$	$4.4 \cdot 10^{-7}$
Permselectivity [-]	1748,11	1263.73	1311.92	1546,95

Prior to the experiments, the inlet gas mixture is bypassed to the analyser to measure the inlet dry gas composition. After this, the feed gas is redirected to the reactor with the permeate side closed to investigate the reaction in a FBR. Steady state operation is quickly reached once the reaction has started. After that, the membrane is unblocked to allow H_2 permeation as in the FBMR configuration a vacuum pump is connected to maximize the driving force and thus, the H_2 permeation through the membrane. Similar experiment is carried out at 450°C to evaluate whether the performance of both reactors can be improved. A model is used to illustrate the performance of both reactors under the same conditions [45].

The outlet composition of the reactor is analysed with the GC, realizing that methane is in the stream. Therefore, SMR reverse reaction and WGS are taking place simultaneously (Ec. 1 and Ec. 2)

The CO conversion is assessing as a function of different experimental conditions for the two different reactor configurations studied in this work (Table 2). The thermodynamic equilibrium is calculated using Aspen Plus V9 and also represented in the main figures presented below in order to check if it is achieved. For all the cases the thermodynamic equilibrium is achieved as it is seen in Figure 22. The performance of the reactor is also studied using a phenomenological model under the same conditions. As it depicted in Figure 22, results obtained with the model are far from the experimental results and the thermodynamic equilibrium, with a much lower CO conversion and thus, lower H_2 production (see graph in the annexure B). In order to interpret the results, it is important to first note that the material of the support is made of Inconel which contains a high percentage of nickel and iron or chromium among others. Since these materials are also used as a catalyst in WGS [57], the difference observed might be related to the support material, which favors the reaction. Practically all CO is converted for all the experiments because the membrane support plays a role as catalyst, while the model just calculates the CO conversion with the catalyst particles.

No huge difference is noticed between both performances of the reactors because of a low driving force in the FBMR case and since similar CO conversion are obtained. In the experimental tests, the vacuum pump used gives a vacuum pressure of 0.3 bar in the permeate side instead of 0, thus leading to a low driving force for H_2 permeation and thus, very low H_2 recovery factor. In FBMR, although the results are quite similar, the H_2 formed permeates through the membrane (shifting the equilibrium to the products and increasing the amount of CO_2 produced) and also, reacts with the CO, producing less methane and steam. Therefore, it is especially interesting to highlight that, according to the model, CO conversion is higher using a FBR rather than FBMR because less amount of H_2 reacts with the CO through the reserve steam methane reforming reaction.

Looking at the effect of the temperature, it is noticed that an increase in temperature implies a higher CO conversion [59]. However, this increase in CO conversion is related to the reverse reforming instead of the direct shift reaction. The difference is more visible in the values obtained with the model. While temperature increases, SMR reaction becomes more favoured than WGS. Due to this fact, there is an increase in CO and H_2 produced, hence the driving force is also increased.

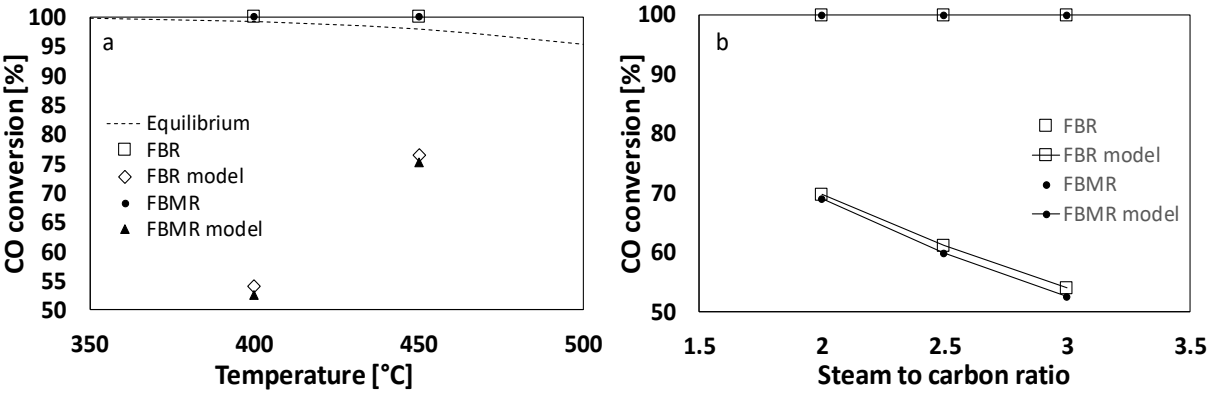

Figure 22. *CO conversion in WGS conditions as a function of a) Temperature, b) Steam to carbon ratio*

When giving a closer inspection to the model results, it is observed that for lower steam to carbon ratios, the CO conversion is lower. This is in contrast with what has been reported in literature [57], where it was claimed that CO conversion increases since the steam to carbon ratio is higher. These unexpected results can be explained for two reasons. The kinetics implemented in the model is the one developed by Numaguchi and Kikuchi [61] whose scheme considers the methane steam reforming and the water gas shift reactions, with a reaction given by:

$$r_{rf} = \frac{k_{rf}\ (p_{CH4}p_{H_2O} - \frac{p_{H_2}^3 p_{CO}}{K_{p,rf}})}{p_{H_2O}^{1.596}} \quad \text{[Ec. 16]}$$

$$r_{wgs} = \frac{k_{wgs}\ (p_{CO}p_{H_2O} - \frac{p_{H_2}p_{CO_2}}{K_{p,wgs}})}{p_{H_2O}} \quad \text{[Ec. 17]}$$

The kinetics demonstrate that increasing the percent of steam, the CO converted decreases. An increase in the steam to carbon ratio implies that the reverse steam methane reforming reaction is less favoured. When steam reacts with CO in the water gas shift reaction H_2 is produced. Then this H_2 can react with CO in the reverse steam methane reaction. However, the excess of the steam in the reactor and thus, the partial pressure of the steam in the reactor, limits the reverse steam methane reforming. This results in a decrease in the consumption of CO moles and therefore, CO converted decreases with a consequent increase in the selectivity to H_2 production.

4.2 Hydrodynamics study

To better understand and predict the behaviour of a fluidized bed membrane reactor operated at high temperatures, better closure equations are required, especially since most of the correlations commonly used in any model are taken from empirical data obtained at room temperatures. In order to investigate the effect of higher temperatures in the behaviour of the emulsion and bubble phases simultaneously, results obtained with the endoscope-laser technique have been compared with LED-PIV/DIA experiments at room temperature to analyse whether different characteristics exist, especially the solid fluxes (SFs) throughout the bed, and others like the bubble diameter and bubble rise velocity. Both methods are described in section 3.3.2.

4.2.1 Comparison LED-PIV/DIA and ePIV/DIA experiments at room temperature

Different experiments have been carried out by Mustafa Taşdemir [1] employing the LED-PIV/DIA technique and by Ildefonso Campos [38] with the novel technique ePIV/DIA. However, the results obtained with the two techniques have not been yet compared in detailed. Their conditions are summarized in the followed Table 8.

Table 8. LED-PIV/DIA and ePIV/DIA experiments conditions

Conditions	***ePIV/DIA***	***LED-PIV/DIA***		
U/U_{mf} [m/s]	2.4	2	3	4
U_g-U_{mf} [m/s]	0.32	0.21	0.42	0.63
d_p (mm)	0.4-0.6		0.4-0.6	
Gas	Nitrogen		Air	
ε_{mf} [-]	0.402		0.379	
U_{mf} [m/s]	0.235		0.21	
T (°C)	20-300		RT	

For the different conditions, the solids fluxes along the bed have been compared. At first, the results at room temperature conditions have been investigated as it can be seen in Figure 23.

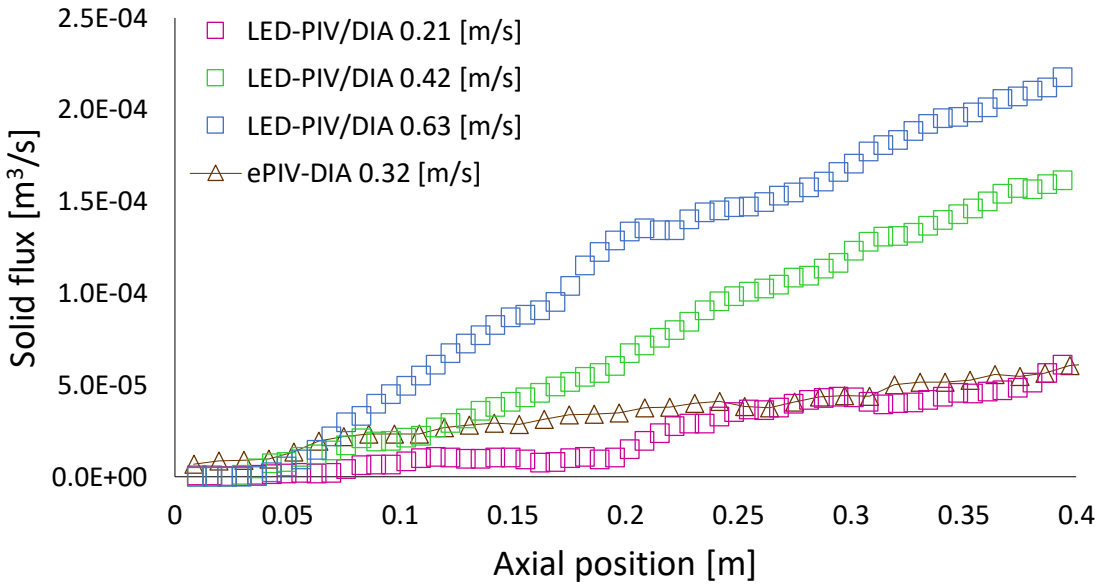

Figure 23. *Solid flows as a function of axial position at different excess gas velocities and techniques at room temperature*

It can be observed that at the bottom of the fluidized bed (0-0.1 m) the solid flux is close to zero. This is due to a limitation of the PIV/DIA technique for having a difficulty to evaluate smaller bubbles than the depth of the column, which are normally present at the bottom of the fluidized bed.

Solid flux obtained with ePIV/DIA is lower than it would be expected. The result is in contrast with what has been reported by Mustafa [1], where it was claimed that for the same particle type, the solid flow is seemingly dependent on the excess gas velocity thus, solid flux obtained with ePIV/DIA should be between LED-PIV/DIA experiments recorded under 0.21 and 0.42 [m/s]. This effect cannot be explained by a different post-processing technique since it is similar for all the experiments, but perhaps associated to the techniques themselves as subsequently explained.

As it has been presented in the previous section, solids fluxes are also strongly dependent on bubble properties. Therefore, they have been compared for the two techniques. It is seen that for bubble diameter depicted in Figure 24, values obtained with LED-PIV/DIA are far smaller than for ePIV/DIA, in contrary what was deemed as in solid fluxes case. Hence, there is a high deviation in the determination of bubble diameter. On the other hand, both techniques give similar bubble rise velocities as it is shown in Figure 25.

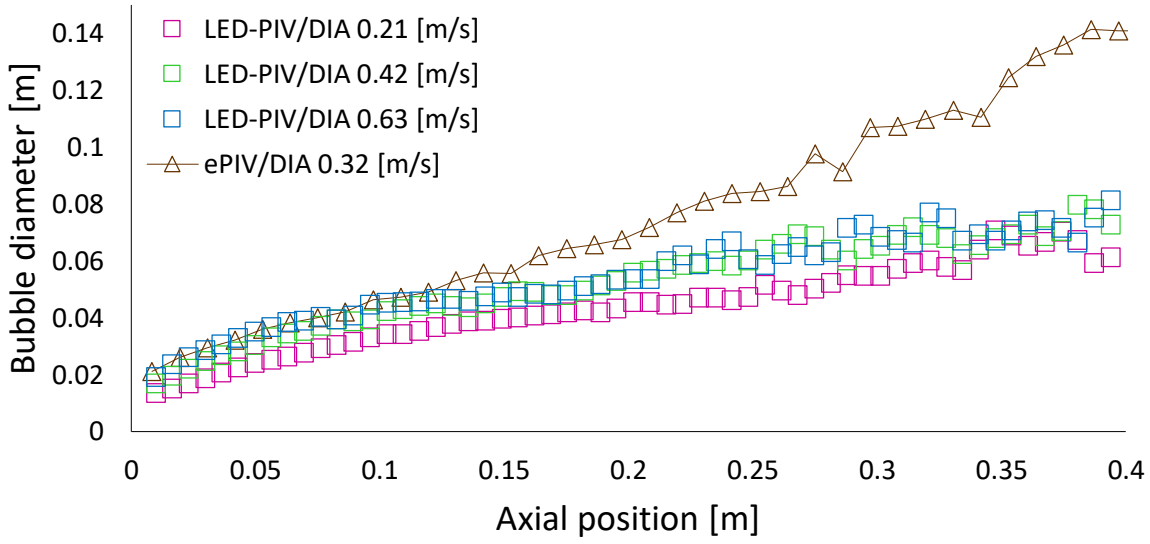

Figure 24. *Bubble diameter as function of bed height at different excess gas velocities and techniques at room temperature*

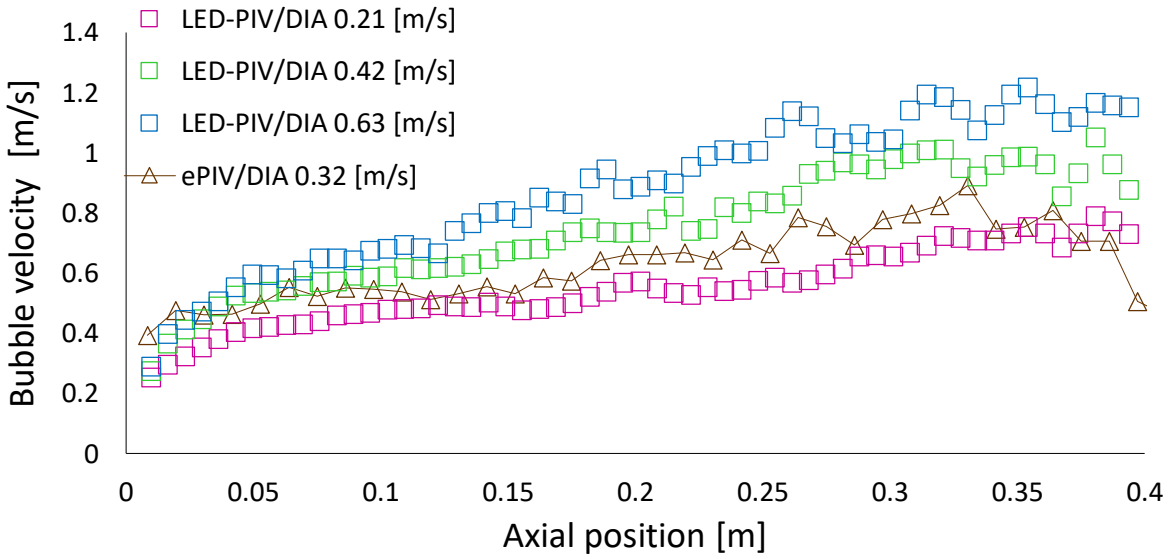

Figure 25. *Bubble velocity as function of bed height at different excess gas velocities and techniques at room temperature*

The main differences between the two techniques are associated to the illumination throughout the bed. Higher intensities might lead to a better contrast between the bubble and emulsion phases, thus helping in the detection of smaller bubbles. This fact has been investigated by the total number of bubbles per image detected by LED-PIV/DIA, which is much higher than for ePIV/DIA as it is shown in Table 9. Therefore, it can be concluded that illumination might be the responsible of the different fluid-dynamic behaviour measured experimentally. It is seemed that the intensity provided by the laser is not high enough to detect the smallest bubbles, since it is wrapped by an endoscope. Thus, less intensity of the beam achieves the wall of the bed. Furthermore, the endoscope is located in a corner

resulting in a weak illumination at the top and bottom right corner of the recorded resulting in an underestimation of the solids hold-up [38].

Table 9. Comparison of number of bubbles detected per image in each technique

Parameter	***ePIV/DIA***		***LED-PIV/DIA***	
nº of bubbles	31656	31313	21654	26731
nº of images recorded	9000	4000	4000	4000
Bubbles/image	3.5	7.83	5.41	6.68

The deviation between both techniques in solid fluxes and bubble diameter data could be accounted to differences in the way of treating the background of the images, implying a different capability to distinguish the bubble and emulsion phases based on pixel intensity after the correction of the inhomogeneous illumination. Therefore, all these aspects lead to treat the recordings taken with LED-PIV/DIA with the script used in ePIV/DIA.

4.2.2 Comparison of LED-PIV/DIA and ePIV/DIA scripts

LED-PIV/DIA images are treated using ePIV/DIA script in order to do a new background and check if the difference in solid fluxes and bubble diameter is a consequence of the way of image normalization.

As described and seen in Figure 26, solid fluxes obtained with both scripts are the same, concluding that there is no a difference in the performance of the background. The same behaviour is encountered in bubble diameter, Figure 27, where it has been noticed a slightly difference between the data treated.

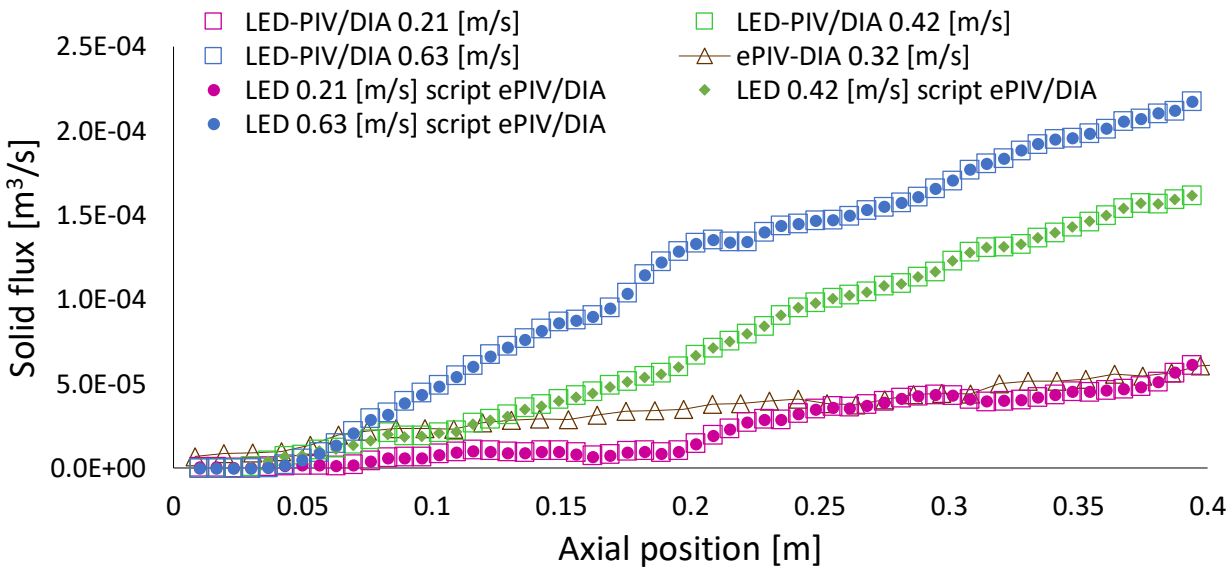

Figure 26. *Comparison of solid fluids obtained with LED-PIV/DIA treated with LED-PIV/DIA script (squares) and with ePIV/DIA script (dots) and obtained with ePIV/DIA(triangle) as function of axial position excess gas velocities at room temperature*

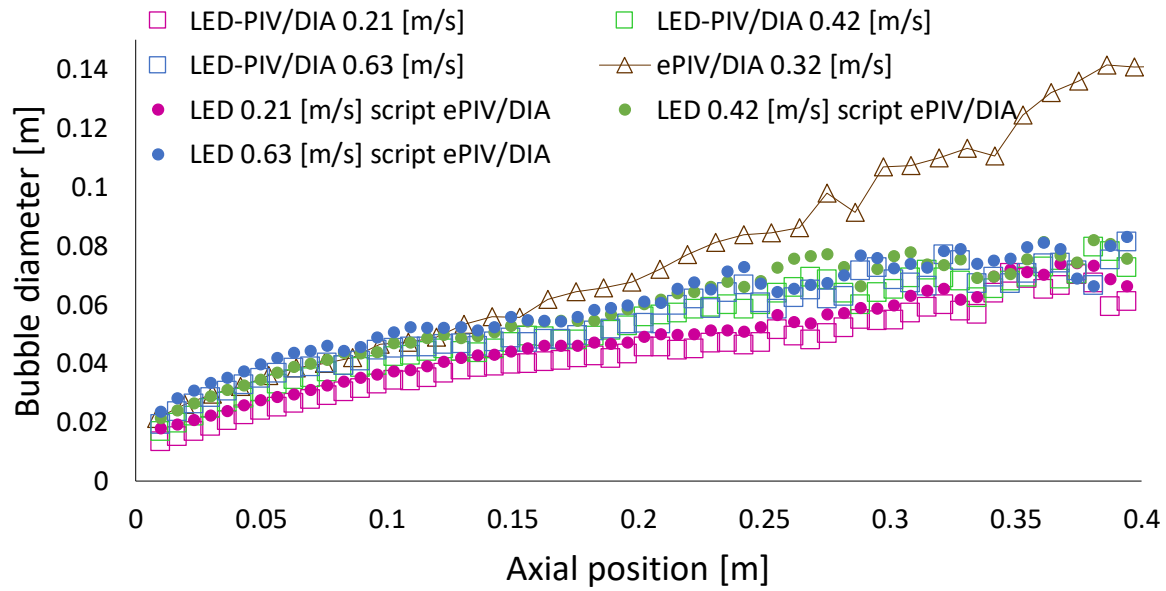

Figure 27. *Comparison of bubble diameter obtained with LED-PIV/DIA treated with LED-PIV/DIA script (squares) and with ePIV/DIA script (dots) and obtained with ePIV/DIA (triangle) as function of axial position excess gas velocities at room temperature*

Both techniques are similar and there is no difference in the way of doing the background (DIA) between the ePIV/DIA and LED-PIV/DIA techniques.. It might be in the way of treating the images and the recordings as well as the intensity of the illumination, said in the previous part.

The detection of the smallest bubbles is hampered if the illumination is not good enough. The intensity of the endoscope that achieve the reactor is less. Therefore, DIA does not take into account the

smallest bubbles, averaging just the biggest. Ildefonso Campos [38] affirms in his thesis that a larger interrogation area is used to treat the images, leading into a decrease in resolution at the bubble-emulsion interface. Averaging the pixel intensity could lead in an overestimation of the bubble diameter and underestimation of solid hold up. Therefore, solid fluxes determined from ePIV/DIA are lower than the estimated with LED-PIV-DIA while bubble diameter is bigger.

Although it has been observed a difference between both techniques, data obtained with ePIV/DIA has been used to determine the solids hold-up at different temperatures using the novel correlation of Mustafa Taşdemir [1] with the aim of extending it to elevated temperatures.

4.2.3 Comparison of ePIV/DIA experiments at different temperatures

The influence of temperature on the hydrodynamics of freely bubbling fluidized beds was studied by Ildefonso Campos using ePIV/DIA [38]. Experiments at constant excess velocities were carried out from room temperature to 300 °C. In this research project, just experiments at 20, 100 and 200 °C are studied due to a change in the fluidization behaviour is observed at 300 °C.

Solid fluxes are determined using the equation 8, where bubble diameter and bubble velocity obtained with ePIV/DIA are used following the procedure described in section 2.2. These values are depicted in Figure 28 along with experimental values at these temperatures and obtained with LED-PIV/DIA.

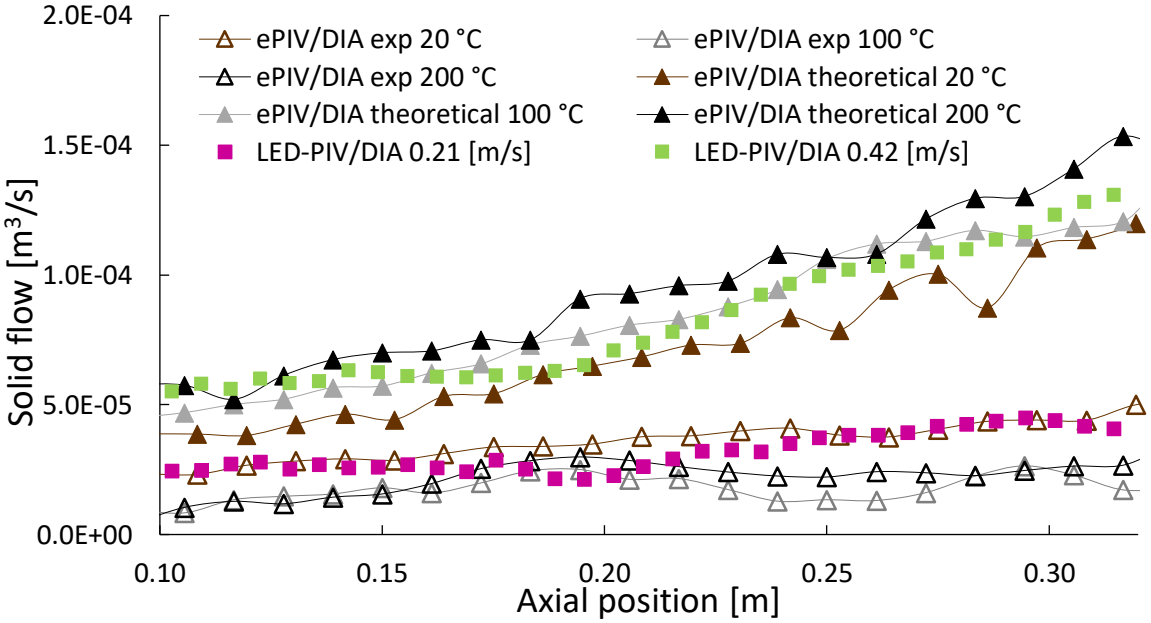

Figure 28. *Experimental (open triangle) and theoretical (closed triangle) solid flows at the same excess gas velocity, 0.32 m/s, at different temperatures compared to SFs obtained in LED-PIV/DIA at different gas velocities at room temperature*

As it has been explaining along this work, since ePIV/DIA experiments were taken under an excess velocity of 0.32 [m/s], experimental and theoretical solid values should be between solid fluxes obtained with LED-PIV/DIA at an excess gas velocity of 0.21 and 0.42 [m/s]. Theoretical data are higher than it was expected. It is a consequence of the imprecise detection of the technique at high temperature, which gives an overestimation of the bubble diameter. Indeed, as it is seen in Figure 28 that while temperature increases, solid fluxes also do because of a slight increase in bubble diameter

and bubble velocity [38] The minimum difference is because the excess velocity remains constant in the data source.

Using the method followed in a previous work [1], a fitting of the experimental value into a theoretical correlation was done. However, the fitting leads to a negative R-square. This means that the experimental error obtained with ePIV/DIA is higher than the one with the model, hindering an appropriated adjust and thus, a development of a new correlation for high temperatures. Therefore, still more research is needed in depth to be able to obtain representative results when using both techniques individually as now, both lead to some differences. In this case, it seems evident that illumination might represent an important challenge when using the ePIV/DIA technique, especially since the interphase between the emulsion and bubble phases becomes less defined as in the case of LED PIV/DIA, which allows higher intensities throughout the bed.

Chapter 5 Conclusions

A Pd-Ag membrane supported on metallic Hastelloy X porous tube with a ceramic layer of Al_2O_3-YSZ in between both layers to prevent interaction has been exposed to hydrogen at low temperatures after a long-term test at 400 ^oC, resulting in membrane embrittlement to remove the Pd-Ag layer. Subsequently, a new ceramic and Pd-Ag layer are deposited on the top of the metallic support following the same procedure as for the fresh supported membrane in order to prove the reutilization of the support.

The repaired membrane has firstly been exposed to single gas permeation tests during more than 700 h between 400 and 500 ^oC. During this period, even though less H_2 permeance and selectivity than for the fresh membrane have been measured, these values are higher than for other metallic membrane supports as reported in literature. An increase in N_2 permeance with the consequence of a pronounced decrease in the ideal perm-selectivity has been observed above 450 ^oC. A deep explanation of the observed decrease is hindered because membrane has not been cut yet after all the set of experiments. However, some hints can be obtained according to superficial roughness studies and N_2 permeances during the membrane time-life. Therefore, according to N_2 permeance test done during the characterization data of the fresh and the repaired membrane, the metallic support might have suffered sintering while the dip coating with the consequence of a decrease in the permeance. Furthermore, since part of the ceramic layer of the fresh support membrane remained after the embrittlement, this layer might become thicker, thus resulting also in a decrease in permeance.

Because the purpose of this work is to give more insights in the feasibility of the FBMR, the membrane has also been tested under the influence of different parameters for WGS reaction. Catalyst interaction with the Pd-Ag layer has not been observed, since the H_2 permeance remains practically constant for single gas test. The reaction was carried out first without the effect of the membrane keeping the permeate side close, followed with the study of the membrane effects once the equilibrium was achieved. No differences between both performances are observed because of the driving force between the reactor and membrane side was not enough. For all the cases, the CO conversion was practically complete, working in a state close to the calculated thermodynamic equilibrium. After a comparison to a model, a catalyst effect of the support material (Inconel) has been observed due to the high CO conversions, besides the effect of the catalyst used. Since this material contains Ni, methanation may occur on the surface of the support, leading in a high purity of H_2.

In order to study the hydrodynamics in a fluidized bed at high temperature, LED-PIV/DIA and ePIV/DIA have firstly been compared at room temperature to verify whether possible differences in the bubble and emulsion phases. While solid fluxes are much higher in the LED PIV/DIA as compared to the ePIV/DIA technique, and the average bubble diameter measured in the endoscopic technique is higher than the ones measured with the technique using LED lights. It might be related to the larger interrogation area used to treat ePIV/DIA recordings as it is depicted in Figure 29. Since ePIV/DIA uses a larger area, if the pixel average is higher than the threshold value, the pixel would be considered as a bubble, when the LED-PIV/DIA would estimate solids and the bubble because of the smaller area.

It leads to a decrease in resolution at the bubble-emulsion interface. Subsequently, ePIV/DIA overestimates bubble diameter detecting larger bubbles and underestimates solids hold-up.

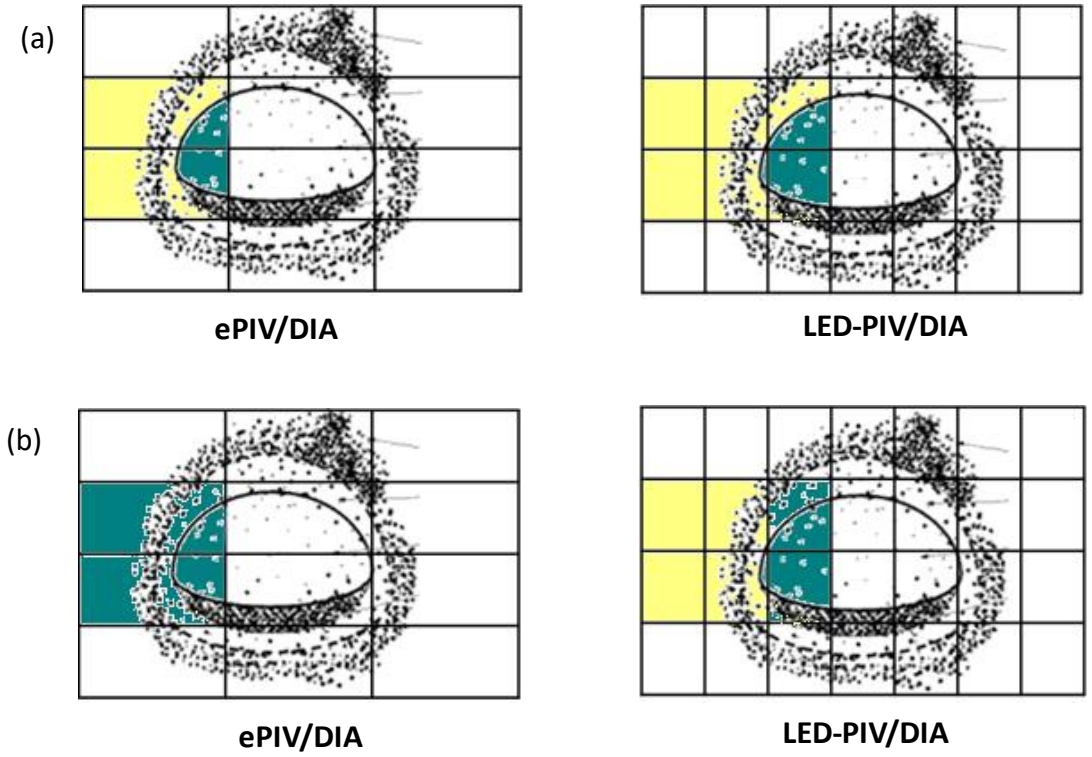

Figure 29. *Estimation of bubbles in each technique according to the size of the area: (a) solids (yellow) and bubble (blue) in each area; (b) bubble and solids estimated by each technique in the area*

Apart from the large area used by ePIV/DIA, the endoscope reduces the intensity of the laser and thus, the illumination is not as good as in LED-PIV/DIA, hampering the detection of the smallest bubbles and averaging the larger bubbles. Furthermore, the endoscope is located in a corner resulting in a weak illumination at the top and bottom right corners and thus, an underestimation of the solids hold-up is found.

The novel correlation to predict solids movement inside fluidized bed as function of bubble properties using PIV/DIA by Mustafa Taşdemir [1] has been used to treat data obtained with ePIV/DIA by Ildefonso Campos with the aim of improving and extending it to elevated temperatures. The deviations observed between both techniques result in a difficult fitting of theoretical and experimental results at high temperature. Also, the correlation should introduce some parameters related to some changes observed at elevated temperatures.

Chapter 6 Recommendations

As it has been discussed in this work, the reutilization of the membrane support might lead into important economic savings when referring to large-scale membrane reactors. Therefore, some further studies should be continued and some recommendations are needed. It must be first considered that this work has been the first it is studied the reutilization of the support and no data are available in order to make some comparison and achieve detailed conclusions.

First, it is observed that the reutilized membrane shows lower H_2 permeances. This could be partly solved by decreasing the thickness of the ceramic layer deposited since part of the original barrier stays in the support. Nevertheless, it could result in an interaction of the Pd layer with the metallic support as it has been demonstrated by other authors [52]. Furthermore, if a small barrier is deposited onto the support, it could also be that the surface roughness is increased and Pd deposition becomes more difficult. Therefore, an exhaustive study might be considered.

Another possibility to improve membrane reparation should be focused on a complete removal of the remaining ceramic barrier, thus leaving the Hastelloy support as similar as the "fresh" one. For a detailed work, an original membrane should be cut in order to analyze the cross-section of the membrane and its surface with the SEM test with the aim of having a reference. Then, using different methods to remove the ceramic layer, the membrane should be tested under the same conditions and subsequently, analyze each membrane using SEM characterization. Even though having identical membranes is a complicated challenge for a good comparison, through the proposed procedure it could be verified whether permeation remains as in the original membrane or it decreases and thus, the causes.

For instance, smoothen should be investigated due to this technique could remove the original ceramic layer, assuring the same roughness as the original fresh support and subsequently, less coatings of ceramic layer would carry out until Rt had a similar value to the original one. In any case, it should be noted that only one membrane has been used in this work and that to get more representative results more samples are needed.

According to the hydrodynamics study, it has been observed that the ePIV/DIA technique uses larger interrogation areas to treat the recordings, hence leading in an overestimation of the bubble diameter detecting larger bubbles and underestimating solids hold-up. Consequently, the interrogation area to treat ePIV/DIA recordings should be reduce in order to improve the pixel averaging and thus, have results more comparable to the ones obtained in the technique using LED lights.

Since the column for the ePIV/DIA technique must be placed inside a closed oven, an endoscope is required to bring the laser beam inside the hot oven and provide the required illumination. However, this endoscope largely reduces the intensity of the laser in the column. Therefore, two possibilities might be considered: the use of a laser with more power, or the use of an endoscope that cuts less energy coming from the laser. In this way the smallest bubbles could also be detected. Also, more studies should be carried out with the aim of placing the laser in front of the reactor in order to have a homogeneous illumination and thus, a better estimation of the solids hold-up.

Until now, the outstanding work carried out be Ildefonso Campos was limited to temperatures up to 300 ^{o}C due to the difficult sealing of the quartz column with the feed line. In order to go to higher temperatures, which will also represent better the behaviour in reaction systems like reforming or water gas shift, a complete reactor made of quartz, including distributor and feed system, might solve these issues. With these studies improved correlations could be obtained, which would lead into more accurate phenomenological models describing fluidized bed (membrane) reactors.

Acknowledgements

I would like to begin by extending my heartfelt gratitude to the Multiphase Reactors Group at Eindhoven University to have given me the opportunity to pursue my graduation project. Thanks to everyone involved in their support during the course of my thesis.

My special regards extend to ir. Jose Medrano, who supervised my project during these months. His constant support and encouragement ensured that my progress was always channelized. It has been a pleasure to have been guided by Jose, whose enthusiasm, extensive knowledge and patience have made this project possible. It would not have been a success without his support and help. The doors to his office were always open and he tried his utter best to provide prompt assistance.

My next and equally important mention would be that of Prof. dr. Martin van Sint Annaland, who made sure that the formalities were never a hindrance in the course of the project. Thank you for steering me towards the right direction and permitting me to join the SMR group to realize this graduation project.

I owe my most sincere gratitude to dr. Fausto Gallucci for his willingness to be part of my graduation committee. A special thanks to Alba Arratibel, who helped me with the characterization of the membranes and Ishan Potdar for the model part. Furthermore, all the other friends and colleagues of the student's room for the great time spent together and made these months feel me like going happily to the university.

I see this project as a stepping stone to my professional journey. I have learnt a lot from the experience and I hope to build upon all the information I have obtained in my future job in the forthcoming months.

References

[1] M. Taşdemir, “Study of Pseudo-2D Fluidized Beds using Optical Techniques: Development of methods for the analyses of the bubble fraction, bubble solids hold-up and the wake fraction,” 2016.

[2] S. D. Angeli, G. Monteleone, A. Giaconia, and A. A. Lemonidou, “State-of-the-art catalysts for CH4 steam reforming at low temperature,” *Int. J. Hydrogen Energy*, vol. 39, no. 5, pp. 1979–1997, 2014.

[3] B. Sorensen, *Hydrogen and fuel cells*, Second Edi. Elsevier Ltd, 2012.

[4] L. Neiva and L. Gama, “The importance of natural gas reforming,” *POTOCNIK, Primoz. Nat. Gas. Sciyo*, pp. 71–87, 2010.

[5] A. M. Adris, C. J. Lim, and J. R. Grace, “The fluidized-bed membrane reactor for steam methane reforming: Model verification and parametric study,” *Chem. Eng. Sci.*, vol. 52, no. 10, pp. 1609–1622, 1997.

[6] H. Amandusson, L. G. Ekedahl, and H. Dannetun, “Effect of CO and O2 on hydrogen permeation through a palladium membrane,” *Appl. Surf. Sci.*, vol. 153, no. 4, pp. 259–267, 2000.

[7] D. Version, “Steam reforming of methane in a membrane reactor : an industrial case study Steam Reforming of Methane in a Membrane Reactor : An Industrial Case Study,” 2017.

[8] S. Tosti *et al.*, “Ethanol steam reforming kinetics of a Pd – Ag membrane reactor,” *Int. J. Hydrogen Energy*, vol. 34, no. 11, pp. 4747–4754, 2009.

[9] D. S. A. Simakov, M. Sheintuch, D. S. A. Simakov, and M. Sheintuch, “Demonstration of a scaled-down autothermal membrane methane reformer for hydrogen generation methane reformer for hydrogen generation,” *Int. J. Hydrogen Energy*, vol. 34, no. 21, pp. 8866–8876, 2009.

[10] F. Gallucci, E. Fernandez, P. Corengia, and M. van Sint Annaland, “Recent advances on membranes and membrane reactors for hydrogen production,” *Chem. Eng. Sci.*, vol. 92, pp. 40–66, 2013.

[11] J. Shu, A. Adnot, B. P. . Grandjean, and S. Kaliaguine, “Structurally stable composite Pd-Ag alloy membranes: Introduction of a diffusion barrier,” *Thin Solid Films*, vol. 286, no. 1–2, pp. 72–79, 1996.

[12] D. Edlund and W. Pledger, “Catalytic platinum-based membrane reactor for removal of H 2 S from natural gas streams,” *J. Memb. Sci.*, vol. 94, pp. 111–119, 1994.

[13] A. G. Knapton, “Palladium Alloys for Hydrogen Diffusion Membranes.,” *Platin. Met. Rev.*, vol. 21, no. 2, pp. 44–50, 1977.

[14] E. Fernandez *et al.*, “Preparation and characterization of metallic supported thin Pd-Ag membranes for hydrogen separation,” *Chem. Eng. J.*, 2015.

[15] A. Tarditi, C. Gerboni, and L. Cornaglia, “PdAu membranes supported on top of vacuum-assisted ZrO2-modified porous stainless steel substrates,” *J. Memb. Sci.*, vol. 428, pp. 1–10, 2013.

[16] H. Li, A. Goldbach, W. Li, and H. Xu, “On CH4 decomposition during separation from H2 mixtures with thin Pd membranes,” *J. Memb. Sci.*, vol. 324, no. 1, pp. 95–101, 2008.

[17] R. Sanz *et al.*, “Preparation, testing and modelling of a hydrogen selective Pd/YSZ/SS composite membrane,” *Int. J. Hydrogen Energy*, vol. 36, no. 24, pp. 15783–15793, 2011.

[18] Ø. Hatlevik, S. K. Gade, M. K. Keeling, P. M. Thoen, A. P. Davidson, and J. D. Way, “Palladium and palladium alloy membranes for hydrogen separation and production: History, fabrication strategies, and current performance,” *Sep. Purif. Technol.*, vol. 73, no. 1, pp. 59–64, 2010.

[19] M. L. Bosko, J. B. Miller, E. A. Lombardo, A. J. Gellman, and L. M. Cornaglia, “Surface characterization of Pd–Ag composite membranes after annealing at various temperatures,” *J. Memb. Sci.*, vol. 369, no. 1, pp. 267–276, 2011.

[20] Z. Dardas, Y. She, T. H. Vanderspurt, J. Yamanis, and C. Walker, “Composite Palladium Membrane Having Long-Term Stability for Hydrogen Separation,” US Patent 00480A1, 2009.

[21] M. L. Bosko, J. F. Múnera, E. A. Lombardo, and L. M. Cornaglia, “Dry reforming of methane in membrane reactors using Pd and Pd–Ag composite membranes on a NaA zeolite modified porous stainless steel support,” *J. Memb. Sci.*, vol. 364, no. 1, pp. 17–26, 2010.

[22] J. A. Calles, R. Sanz, and D. Alique, “Influence of the type of siliceous material used as intermediate layer in the preparation of hydrogen selective palladium composite membranes over a porous stainless steel support,” *Int. J. Hydrogen Energy*, vol. 37, no. 7, pp. 6030–6042, 2012.

[23] L. Wei, J. Yu, X. Hu, and Y. Huang, “Fabrication of H2-permeable palladium membranes based on pencil-coated porous stainless steel substrate,” *Int. J. Hydrogen Energy*, vol. 37, no. 17, pp. 13007–13012, 2012.

[24] J. A. Medrano, F. Boccia, N. Alfano, F. Gallucci, and M. V. S. Annaland, “Mass transfer in bubbling beds using a novel whole field high temporal resolution Infra-Red technique.”

[25] P. Lettieri, J. G. Yates, and D. Newton, “The influence of interparticle forces on the fluidization behaviour of some industrial materials at high temperature,” *Powder Technol.*, vol. 110, no. 1–2, pp. 117–127, 2000.

[26] D. Kunii, *Fluidization engineering*, Second Edi. 1991.

[27] K. Yoshida and C. Y. Wen, “Noncatalytic solid-gas reaction in a fluidized reactor,” *Chem. Eng. Sci.*, vol. 25, no. 9, pp. 1395–1404, 1970.

[28] I. C. Velarde, F. Gallucci, and M. van Sint Annaland, “Development of an endoscopic-laser PIV/DIA technique for high-temperature gas-solid fluidized beds,” *Chem. Eng. Sci.*, vol. 143, pp. 351–363, 2016.

[29] V. Wiesendorf and J. Werther, “Capacitance probes for solids volume concentration and velocity measurements in industrial fluidized bed reactors,” *Powder Technol.*, vol. 110, no. 1–2, pp. 143–157, 2000.

[30] J. Werther, “Measurement Techniques in Fluidized Beds,” *Powder Technol.*, vol. 102, no. July 1998, pp. 15–36, 1999.

[31] J. Chaouki, F. Larachi, and M. P. Dudukovic, “Noninvasive Tomographic and Velocimetric Monitoring of Multiphase Flows,” *Ind. Eng. Chem. Res.*, vol. 5885, no. 418, pp. 4476–4503, 1997.

[32] A. Laverman, *On the hydrodynamics in gas polymerization reactors*. Eindhoven: Eindhoven University of Technology, 2010.

[33] J. F. Davidson and D. Harrison, *Fluidised Particles*. New York, 1963.

[34] C. Chavarie and J. R. Grace, “Interphase mass transfer in a gas fluidized bed,” *Chem. Eng. Sci.*, vol. 31, no. 9, pp. 741–749, 1976.

[35] P. N. Rowe and B. A. Partridge, “Cloud formation around bubbles in gas fluidized beds,” vol. 19, pp. 973–985, 1964.

[36] R. Radmanesh, C. Guy, R. Radmanesh, R. Mabrouk, J. Chaouki, and C. Guy, “I NTERNATIONAL J OURNAL OF C HEMICAL Effect of Temperature on Solids Mixing in a Bubbling Fluidized Bed Reactor Effect of Temperature on Solids Mixing in a Bubbling Fluidized Bed Reactor,” vol. 3, 2005.

[37] S. Rapagna, P. U. Foscolo, and L. G. Gibilaro, “The influence of temperature on the quality of gas fluidization,” *Int. J. Multiph. Flow*, vol. 20, no. 2, pp. 305–313, 1994.

[38] I. C. Velarde, “High temperature hydrodynamics for chemical looping biomass gasification,” Eindhoven University of Technology, 2016.

[39] E. Wicke, H. Brodowsky, and H. Zu¨ chner, “Hydrogen in metals II,” V. J. Alefeld G, Ed. Berlin, 1978, pp. 73–155.

[40] “Correlations in palladium membranes for hydrogen separation : A review,” 2009.

[41] D. Kunii and O. Levenspiel, *Bubbling bed model*. I&EC Fundam, 1968.

[42] S. Ergun, *Fluid flow through packed columns*. Chem. Eng. Prog, 1952.

[43] J. R. Grace, *Contacting modes and behaviour classification of gas solid and other two phase suspensions*. Can. J. Chem. Eng.

[44] S. Mori and C. Y. Wen, *Estimation of bubble diameter in gaseous fluidized beds*. AlChE, 1975.

[45] A. Battistella, "Membrane assisted chemical looping reforming process modeling for H2 production," Eindhoven, 214AD.

[46] I. Iliuta, R. Tahoces, G. S. Patience, S. Rifflart, and F. Luck., *Chemical-Looping Combustion Process: Kinetics and Mathemtical Modeling*. AIChE Journal, 2010.

[47] D. L. F. Brown and H. S. Fogler., "Diffusion and reaction in porous catalysts," 2008. [Online]. Available: http://umich.edu/~elements/12chap/html/12prof2a.htm. [Accessed: 08-Nov-2016].

[48] P. N. Rowe and A. J. Widmer, "Variation in shape with size of bubbles in fluidised beds," *Chem. Eng. Sci.*, vol. 28, no. 3, pp. 980–981, 1973.

[49] D. A. Pacheco Tanaka, M. A. Llosa Tanco, J. Okazaki, Y. Wakui, F. Mizukami, and T. M. Suzuki, "Preparation of 'pore-fill' type Pd-YSZ-??-Al2O3 composite membrane supported on ??-Al2O3 tube for hydrogen separation," *J. Memb. Sci.*, vol. 320, no. 1–2, pp. 436–441, 2008.

[50] D. A. Pacheco *et al.*, "Preparation of palladium and silver alloy membrane on a porous ⌴ -alumina tube via simultaneous electroless plating," vol. 247, pp. 21–27, 2005.

[51] J. R. Rostrup-nielsen, "Coking on Nickel Catalysts for Steam Reforming of Hydrocarbons," vol. 201, pp. 184–201, 1974.

[52] J. A. Medrano *et al.*, "Pd-based metallic supported membranes: High-temperature stability and fluidized bed reactor testing," *Int. J. Hydrogen Energy*, vol. 41, no. 20, pp. 8706–8718, 2016.

[53] "Coupled PIV/DIA for fluid dynamics studies on a Two-Section Two-Zone Fluidized Bed Reactor," *Chem. Eng. J.*, vol. Julian, I;, pp. 122–132, 2012.

[54] M. S. van Buijtenen, M. Börner, N. G. Deen, S. Heinrich, S. Antonyuk, and J. A. M. Kuipers, "An experimental study of the effect of collision properties on spout fluidized bed dynamics," *Powder Technol.*, vol. 206, no. 1–2, pp. 139–148, 2011.

[55] J. F. de Jong, S. O. Odu, M. S. van Buijtenen, N. G. Deen, M. van Sint Annaland, and J. A. M. Kuipers, "Development and validation of a novel Digital Image Analysis method for fluidized bed Particle Image Velocimetry," *Powder Technol.*, vol. 230, pp. 193–202, 2012.

[56] B. Dittmar, A. Behrens, N. Scho, M. Ru, G. Straczewski, and R. Dittmeyer, "Methane steam reforming operation and thermal stability of new porous metal supported tubular palladium composite membranes," vol. 8, 2013.

[57] S. Liguori *et al.*, "Performance of a Pd / PSS membrane reactor to produce high purity hydrogen via WGS reaction," *Catal. Today*, vol. 193, no. 1, pp. 87–94, 2012.

[58] L. Shi, A. Goldbach, and H. Xu, “High-flux H 2 separation membranes from (Pd / Au) n nanolayers,” *Int. J. Hydrogen Energy*, vol. 36, no. 3, pp. 2281–2284, 2010.

[59] A. Helmi, E. Fernandez, J. Melendez, D. A. P. Tanaka, F. Gallucci, and M. Van Sint Annaland, “Fluidized bed membrane reactors for ultra pure H2 production - A step forward towards commercialization,” *Molecules*, vol. 21, no. 3, 2016.

[60] F. Gallucci, F. Chiaravalloti, S. Tosti, E. Drioli, and A. Basile, “The effect of mixture gas on hydrogen permeation through a palladium membrane: Experimental study and theoretical approach,” *Int. J. Hydrogen Energy*, vol. 32, no. 12, pp. 1837–1845, 2007.

[61] T. Numaguchi and K. Kikuchi, “Intrinsic kinetics and design simulation in a complex reaction network; steam-methane reforming,” *Chem. Eng. Sci.*, vol. 43, no. 8, pp. 2295–2301, 1988.

Annexure

A. Micro Gas Chromatograph calibrations

CO/N_2

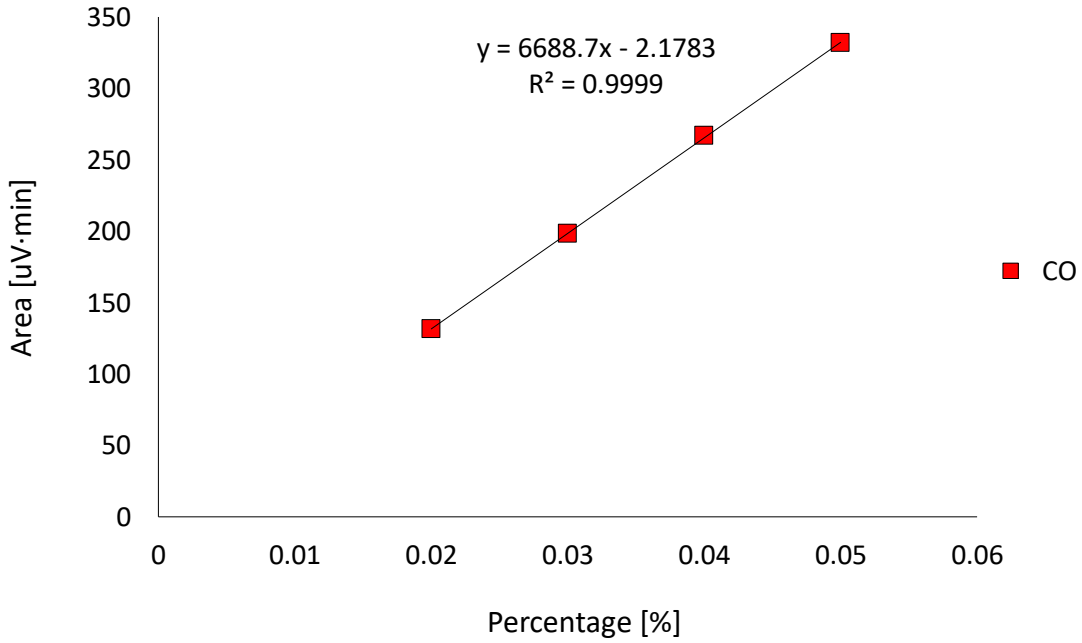

$H_2/CO_2/N_2$

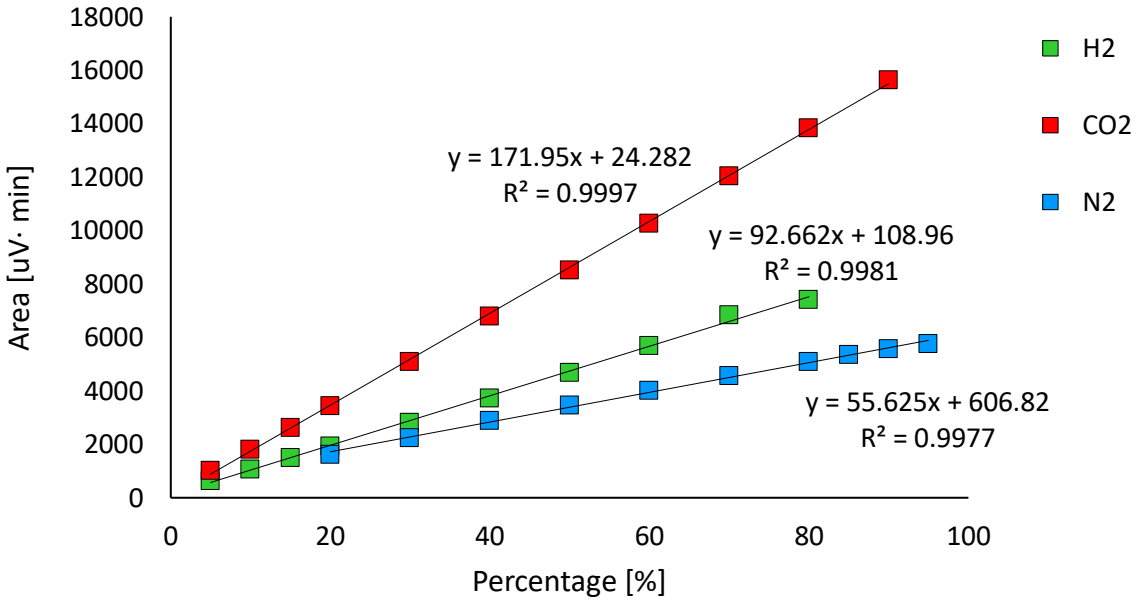

CH_4/CO_2

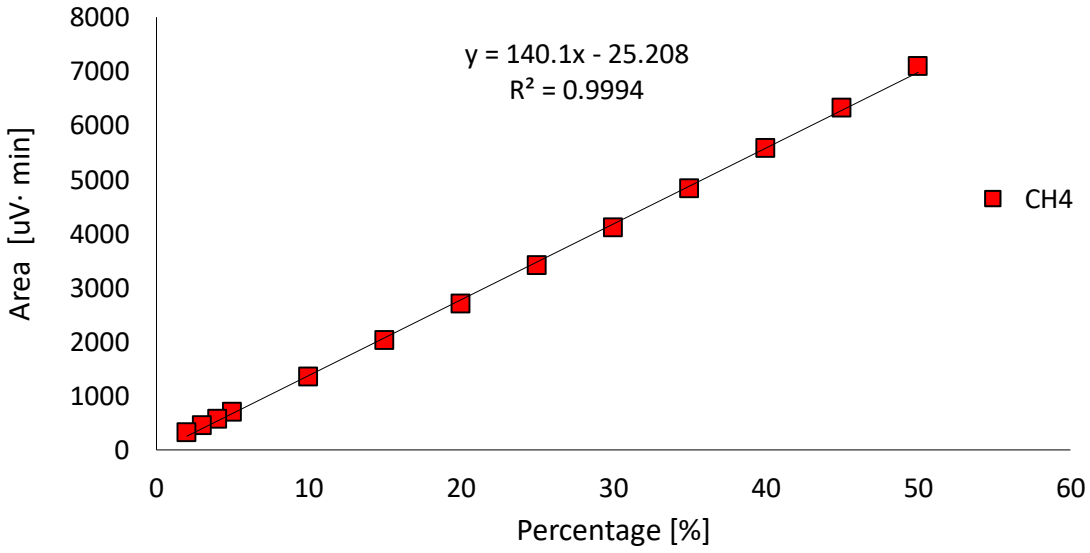

B.Water gas shift

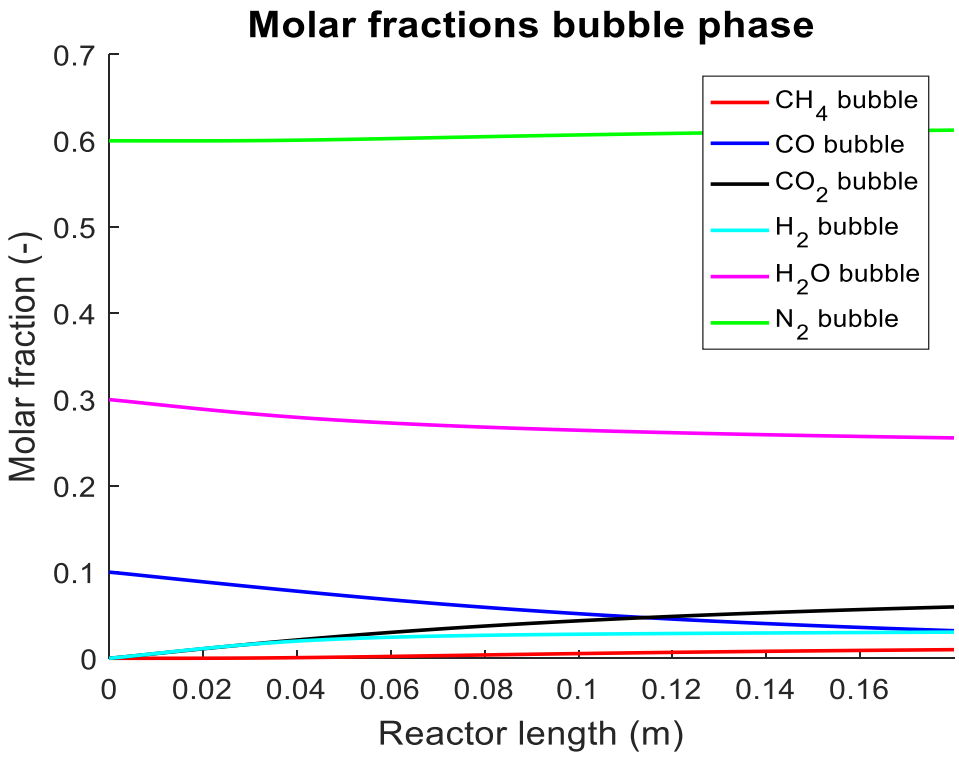

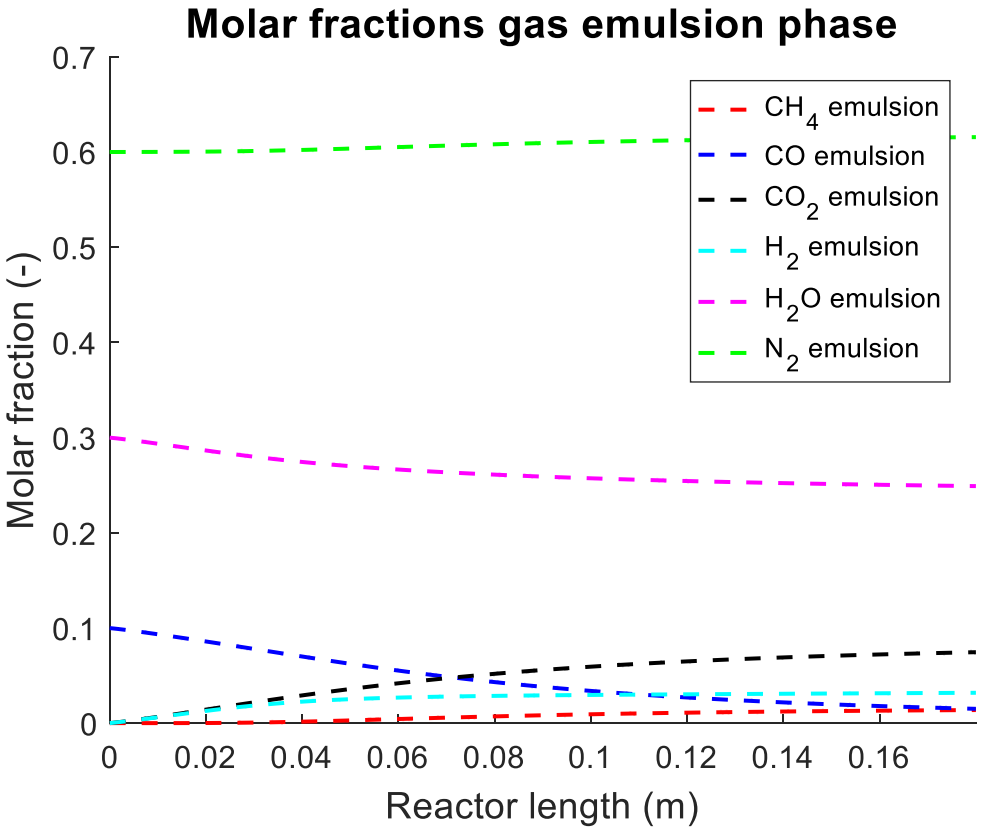
Molar fractions gas emulsion phase
Molar fraction (-)
Reactor length (m)
0.7
0.6
0.5
0.4
0.3
0.2
0.1
0
0
0.02
0.04
0.06
0.08
0.1
0.12
0.14
0.16
CH4 emulsion
CO emulsion
CO2 emulsion
H2 emulsion
H2O emulsion
N2 emulsion